

Macroscopic Dark Matter under siege: from White Dwarf Data to Gravitational Wave Detection

Siyu Jiang,¹ Aidi Yang,¹ and Fa Peng Huang^{1,*}

¹*MOE Key Laboratory of TianQin Mission, TianQin Research Center
for Gravitational Physics & School of Physics and Astronomy,
Frontiers Science Center for TianQin, Gravitational Wave Research Center of CNSA,
Sun Yat-sen University (Zhuhai Campus), Zhuhai 519082, China*

The nature of dark matter (DM) remains a profound mystery. Macroscopic candidates, such as Fermi-balls, offer a distinct alternative to conventional particle DM, yet their low number density makes terrestrial detection challenging. In this work, we present a unified search strategy for sub-saturated Fermi-ball DM. We first revisit and significantly update astrophysical constraints from compact objects, utilizing rigorous expressions and additional white dwarf data related to ignition and subsequent supernovae. Crucially, we then explore novel signatures of Fermi-balls in future gravitational wave experiments like LISA and TianQin, performing detailed signal-to-noise ratio and Fisher matrix analyses. By combining these updated white dwarf/neutron star limits with the projected gravitational wave sensitivities, we derive the most comprehensive constraints on Fermi-ball parameter space to date, demonstrating the power of multi-messenger approaches for probing macroscopic DM.

As one of the most profound mysteries in the universe, the properties of dark matter (DM) have long been explored by physicists. In addition to particle and wave-like DM, there are also motivations suggesting that DM may be formed through the composition of dark particles, analogous to the formation of atoms from electrons and protons in the visible world. The typical candidates of this species of DM are Q-ball or Fermi-ball, which may be formed through Affleck-Dine mechanism [1, 2] or a first-order phase transition [3–7].

For these macroscopic DM candidates, due to their low number density in the universe, it is hard to detect them on terrestrial experiments like direct detection experiments. Many efforts for detecting them have been proposed [8–14]. The astrophysical compact objects like white dwarfs (WDs) and neutron stars (NSs) provide powerful probes for detecting macroscopic DM. When a macroscopic DM transits the white dwarfs, it may transfer enough energy in terms of the scattering to trigger runaway fusion and ignite a type Ia supernova [15, 16]. The astrophysical constraints on macroscopic DM have been reconsidered [17, 18]. In addition, for relatively lighter DM with mass $m_{\text{DM}} \sim \mathcal{O}(1 - 10^6)$ GeV, compact objects also have the ability to constrain their properties by capturing them [19–30]. For instance, the captured asymmetric DM could accrete to trigger gravitational collapse of compact objects into a black hole [31–37]. For symmetric DM, DM annihilation can heat NSs and produce radiation detectable by telescopes [38–40].

Furthermore, DM yields unique signatures in gravitational wave (GW) experiments [41–54]. For a review, see [55]. Macroscopic DM could interact directly with the satellites [41–46], or affect the photon propagation through the Shapiro effect [56–61].

In this letter, we revisit the astrophysical constraints (supernovae and superbursts) on Fermi-ball DM by uti-

lizing rigorous expressions and more WD data. In addition, we investigate the direct signals of Fermi-ball DM in GW detectors like LISA [62] and TianQin [63].

Fermi-ball DM with long-range interaction—We consider the minimal Fermi-ball DM model by simply introducing a scalar ϕ and a fermion X beyond the standard model (SM) [64],

$$\mathcal{L} = \frac{(\partial\phi)^2}{2} - \frac{1}{2}m_\phi^2\phi^2 + \bar{X}i\not{\partial}X - m_X\bar{X}X + y_X\bar{X}\phi X. \quad (1)$$

We fix $m_X = 100$ GeV. When the scalar field ϕ varies slowly over the Compton wavelength of X , it can be treated as a classical background field that induces a spatially varying effective mass $m_X - y_X\phi(\mathbf{r})$ for X . Within the Thomas-Fermi approximation, the X particles are treated as a degenerate Fermi gas. The total energy of the $X - \phi$ system with radius R_X is

$$E_X(\phi(\mathbf{r}), k_F(\mathbf{r})) = 4\pi \int_0^{R_X} dr r^2 \left\{ \frac{1}{2} [(\nabla\phi)^2 + m_\phi^2\phi^2] + \frac{g_X}{2\pi^2} \int_0^{k_F} dk k^2 \sqrt{k^2 + (m_X - y_X\phi)^2} \right\}, \quad (2)$$

where the Fermi-ball is assumed to be spherical. g_X is the degree of freedom of X and k_F is the Fermi momentum. The fermion number is defined by

$$N_X = \int d^3\mathbf{r} \langle X^\dagger X \rangle = \frac{2g_X}{3\pi} \int_0^{R_X} dr r^2 k_F^3. \quad (3)$$

Using the minimization condition, $\delta E_X - \mu \delta N_X = 0$ with μ being the chemical potential, one gets the relation $\mu = \frac{\delta E_X / \delta k_F(r)}{\delta N_X / \delta k_F(r)} = \sqrt{k_F^2(r) + [m_X - y_X\phi(r)]^2}$. The numerical and analytical analyses of the Fermi-ball profile are shown in the Supplementary Material.

We investigate the case where the constituents are relativistic for large fermion number N_X , but $R_X <$

m_ϕ^{-1} [64]. The Fermi-ball in this case is “sub-saturated” and has the scaling $R_X \sim N_X^{2/3}$, or more precisely,

$$N_X = \frac{2g_X}{9\pi} \left(\frac{3\pi m_X^2}{g_X \alpha_X} \right)^{3/4} R_X^{3/2}, \quad (4)$$

with $\alpha_X = y_X^2/4\pi$, and

$$M_X = N_X \mu = \frac{2}{3} \frac{m_X^2}{\alpha_X} R_X. \quad (5)$$

It can be seen from Eqs. (4) and (5) that $M_X \propto N_X^{2/3}$, therefore the Fermi-ball mass grows slower than N_X . This implies the existence of a negative binding energy, which renders the Fermi-ball more stable than a system of N_X free fermions and provides the possibility for Fermi-ball to serve as the DM candidate.

Assuming the scalar ϕ also couples to the SM sector — for instance, to nucleons via $y_n \bar{n} \phi n$ — an additional Yukawa attractive potential arises between two objects $i, j \in \{\text{SM}, X\}$,

$$V_{i-j} = -M_i M_j \frac{G}{r} (1 + \delta_i \delta_j e^{-m_\phi r}), \quad (6)$$

with $\delta_i = \frac{\sqrt{\alpha_i}}{\sqrt{G \bar{m}_i}}$. $\bar{m}_i = M_i/N_i$ is the averaged mass per constituent and $\alpha_{\text{SM}} = y_n^2/4\pi$. It is obvious that $\bar{m}_X = \mu$ for Fermi-ball DM, and we set \bar{m}_n to be the nucleon mass for nucleons. From Eqs. (4) and (5), the DM effective coupling reads,

$$\delta_X = \left(\frac{g_X \alpha_X^5 M_X^2}{4\pi G^2 m_X^6} \right)^{1/4} = \frac{2}{3} \left(\frac{m_X^4 R_X^5}{3\pi G^2 M_X^3} \right)^{1/4}. \quad (7)$$

While $|\delta_{\text{SM}}| < 3 \times 10^{-6}$ has been strongly constrained by the MICROSCOPE mission’s weak equivalence principle test [65, 66], the DM coupling could be several orders larger, since the only relevant constraints are imposed by the influence of DM self-interaction on structure formation [67–69]. Observation of the bullet cluster constrained the cross- of DM to be $\sigma/M_X \lesssim 1 \text{ cm}^2/\text{g}$, from which the constraint on δ_X is given by [70]:

$$\delta_X^2 < 2 \times 10^6 \left(\frac{M_X}{M_\odot} \right)^{-1/2} \left(\frac{v_{\text{DM}}}{10^{-2}} \right)^2 e^{4 \times 10^{-3} \sqrt{\frac{M_X}{M_\odot}} \frac{\text{pc}}{X}}, \quad (8)$$

with $\lambda = m_\phi^{-1}$ and v_{DM} the DM velocity. From the definition of number density $n_X \equiv d_X^{-3} = \rho_X/M_X$ with ρ_X the energy density of Fermi-ball DM, the characteristic distance between the Fermi-ball DM reads,

$$d_X \simeq 1.2 \times 10^4 \text{ km} \times f_X^{-1/3} \left(\frac{M_X}{1 \text{ kg}} \right)^{1/3}, \quad (9)$$

where we have assumed that the Fermi-ball accounts for only a part of the total DM, $\rho_X = f_X \rho_{\text{DM}}$ with

$\rho_{\text{DM}} = 0.4 \text{ GeV/cm}^3$ being the DM density. This is phenomenologically reasonable in the theory of Fermi-ball formation during a first-order phase transition [6]. We will also assume the force range of sub-saturated Fermi-ball is larger than the typical lengths in this work, i.e., the radius of the WD or NS, and the arm length of the GW detector; for instance, we take $\lambda = 0.1 \text{ pc}$. Then the attractive potential between the DM and the nucleons is simply obtained by replacing the Newton constant in the gravitational potential by $G \rightarrow G(1+\tilde{\alpha})$ with $\tilde{\alpha} = \delta_{\text{SM}}\delta_X$.

Runaway fusion of compact objects— Firstly, we briefly discuss the condition of triggering runaway fusion in a WD core and NS ocean. When DM passes a WD or an NS, it may deposit energy through scattering with C or O ions. If the energy deposition E_{dep} is enough for the ions to overcome their mutual Coulomb barrier, the runaway fusion occurs. Therefore, the first condition for fusion is that the energy deposition must raise the temperature of a certain area above some critical value $T_{\text{crit}} \sim \text{MeV}$. In this work, T_{crit} is set to be 0.5 MeV [71]. The second condition is that the timescale for cooling due to thermal diffusion has to be longer than the timescale corresponding to the heating due to fusion. The former increases with the size of the heated region but the latter is independent of the size of the region; therefore, there is a critical size λ_T beyond which the heat cannot be efficiently diffused [16]. Following the discussion in [72], the ignition condition reads,

$$E_{\text{dep}} \geq \frac{4\pi}{3} \rho \lambda_T^3 (\rho, T_{\text{crit}}) \bar{c}_p (\rho, T_{\text{crit}}) T_{\text{crit}}, \quad (10)$$

where ρ is the local density of WDs or NSs. $\bar{c}_p \simeq c_p^{\text{ion}}/2 + c_p^\gamma/4 + c_p^e$ is the averaged heat capacity with the heat capacity for ions, photons, and electrons (see Supplementary Material).

It is often assumed that the DM triggers the ignition near the center of a CO WD. Obtaining the precise density profile of WDs requires solving the Tolman–Oppenheimer–Volkoff (TOV) equation [73, 74]. In this work, we use the analytic fit of the WD-mass central density relationship introduced by Ref. [72],

$$\left(\frac{\rho_{\text{WD}}}{1.95 \times 10^6 \text{ g/cm}^3} \right)^{2/3} + 1 \approx \left[\sum_{i=0}^6 c_i \left(\frac{M_{\text{WD}}}{M_\odot} \right)^i \right]^{-2} \quad (11)$$

with $\{c_i\} = \{1.0033, -0.3087, -1.1652, 2.0211, -2.0604, 1.1687, -0.2810\}$.

The trigger length λ_T is obtained by comparing the nuclear energy generation rate and the heat diffusion rate. However, the specific nuclear energy generation rates of the WD generally require numerical simulation, and the Ref. [72] provides an analytical scaling relation,

$$\lambda_T = \begin{cases} \lambda_1 \left(\frac{\rho}{\rho_1} \right)^{-2}, & \rho \leq \rho_1, \\ \lambda_1 \left(\frac{\rho}{\rho_1} \right)^{\ln(\lambda_2/\lambda_1)/\ln(\rho_2/\rho_1)}, & \rho_1 < \rho \leq \rho_2 \end{cases} \quad (12)$$

with $\{\lambda_1, \lambda_2\} = \{1.3 \times 10^{-4} \text{ cm}, 2.5 \times 10^{-5} \text{ cm}\}$ and $\{\rho_1, \rho_2\} = \{2 \times 10^8 \text{ g} \cdot \text{cm}^{-3}, 10^{10} \text{ g} \cdot \text{cm}^{-3}\}$ for WDs. We take 4361 WDs in Montreal White Dwarf Database [75] with known lifetimes and masses spanning $0.8 < M_{\text{WD}}/M_{\odot} < 1.4$. The minimum trigger length is found to be $\lambda_T \approx 4.8 \times 10^{-5} \text{ cm}$.

Unlike WDs, the thermal nuclear runaway causes the NSs to undergo a superburst instead of a supernova. The outer layer of NS consists of an ocean of heavy elements, where the mass fraction of carbon is approximately 10% [76]. For NSs, we assume the relation (12) still holds. The superbursts source 4U 1820-30 is used to place constraints on the Fermi-ball DM. The mass and radius of the NS are [77] $M_{\text{NS}} = 1.58 M_{\odot}$ and $R_{\text{NS}} = 9.11 \text{ km}$ respectively. The recurrence time of 4U 1820-30 is taken to be $t_{\text{rec}} = 2.5 \text{ yr}$ [17] and its Galactic position is 1.2 kpc. The trigger length of NS is derived by integrating the neutron star crust density profile in Ref. [78] to obtain the crustal column depth and then comparing it to the maximum ignition column depth of $4 \times 10^{13} \text{ g} \cdot \text{cm}^{-2}$ presented in Fig. 1 of Ref. [76].

As the Fermi-ball DM passes through a compact object with mass M_{CO} and radius R_{CO} , it can deposit its energy through elastic scattering. The energy transfer reads,

$$\frac{dE_{\text{dep}}}{dx} \approx \rho \sigma_{XA} v_{\text{esc}}^2 (1 + \tilde{\alpha}), \quad (13)$$

where $\sigma_{XA} \simeq \pi R_X^2$ is the scattering cross between DM and carbon ions. $v_{\text{esc}} = \sqrt{2GM_{\text{CO}}/R_{\text{CO}}}$ is the escape speed on the surface of compact objects. Given that $R_X \gg \lambda_T$, we have to multiply E_{dep} by $(\lambda_T/R_X)^3$ after taking into account the energy deposition in the critical volume, $\frac{4\pi}{3} \lambda_T^3$. Then the energy deposition to trigger the ignition reads,

$$E_{\text{dep}} \simeq \pi \rho R_X^3 v_{\text{esc}}^2 (1 + \tilde{\alpha}) \left(\frac{\lambda_T}{R_X} \right)^3. \quad (14)$$

Astrophysical constraints from supernova and superburst.— In addition to the ignition, it is important to investigate the event rate at WDs/NSs. The encounter rate between DM and WD/NS relies on the maximum impact factor b_{max} [70], whose complete formula can be found in Supplementary Material. The encounter rate between DM and compact objects is defined by

$$\Gamma_{\text{enc}}^X(r) = f_X \frac{\rho_{\text{DM}}(r)}{M_X} v_{\text{DM}}(r) \pi b_{\text{max}}^2. \quad (15)$$

For WDs, DM is chosen to be at the solar position, $r_{\odot} = 8.3 \text{ kpc}$, where $\rho_{\text{DM}}(r_{\odot}) = 0.4 \text{ GeV/cm}^3$ and $v_{\odot} \approx 220 \text{ km/s}$ [79–82].

The expected number of DM passing through the WDs is

$$N_{\text{enc}}^{\text{WD}} = \sum_i \Gamma_{\text{enc}}^X \tau_{\text{WD},i}. \quad (16)$$

We set $N_{\text{enc}}^{\text{WD}} = 3$ which may be ruled out at 95% confidence, as pointed in Ref. [17]. For NSs, the τ_{WD} has to be replaced by t_{rec} . In order to evaluate the DM velocity at the position of NS, we use the Maxwell-Boltzmann dispersion speed $v_{\text{DM}}(r) = \sqrt{3GM(r)/2r}$ where $M(r)$ is the DM mass enclosed in r [18]. By adopting the Navarro-Frenk-White profile [83, 84],

$$\rho_{\text{DM}}(r) = \frac{\rho_c}{\left(\frac{r}{r_s}\right) \left(1 + \frac{r}{r_s}\right)^2}, \quad (17)$$

where $r_s = 20 \text{ kpc}$ and ρ_c can be fixed by $\rho_{\text{DM}}(r_{\odot})$, then $M(r) = \int_0^r d^3\mathbf{r}' \rho_{\text{DM}}(r')$.

For WDs, there will be a surface above which the electrons become non-degenerate, and there the density ρ_{env} is typically only about 0.1% of the central density. The temperature T_* at the transition point can be determined by equating the electron pressure of the degenerate layer to that of the non-degenerate layer [85]. More details can be found in the Supplementary Material. Then the radius R_* at which $T = T_*$ can be obtained from

$$T_* = \frac{1}{4.25} \frac{\bar{\mu} \mu_a}{k} \frac{GM_{\text{WD}}}{R_{\text{WD}}} \left(\frac{R_{\text{WD}}}{R_*} - 1 \right), \quad (18)$$

where μ_a is the atomic mass unit. And $\bar{\mu} \equiv (\sum_i X_i(1 + Z_i)/A_i)^{-1}$ is the mean molecular weight with X_i , Z_i , and A_i being the mass fraction, charge, and atomic mass number of ion species i , respectively. The width of a non-degenerate WD envelope is defined by $R_{\text{env}} = R_{\text{WD}} - R_*$. The condition for DM to penetrate into the WDs is that the energy loss of DM cannot exceed the incident kinetic energy of DM,

$$\frac{dE_{\text{dep}}}{dx} \approx \rho_{\text{env}} \sigma_{XA} v_{\text{esc}}^2 (1 + \tilde{\alpha}) < \frac{M_X v_{\text{esc}}^2 (1 + \tilde{\alpha})}{R_{\text{env}}}. \quad (19)$$

From which one can obtain $\frac{\sigma_{XA}}{M_X} < \frac{1}{\rho_{\text{env}} R_{\text{env}}}$. We take ρ_{env} to be 10^{-3} of the central density, $\rho_{\text{env}} = 10^{-3} \rho_{\text{WD}}$. From the updated WD database and the rigorous analyses above we obtain a conservative bound $\sigma_{XA}/M_X > 7.3 \times 10^{-11} \text{ cm}^2/\text{g}$ that is shown in Fig. 1. This value is about 100 times larger than that in [16] and 10^6 times larger than the value reported in [17], but it is 300 times smaller than the value in [18].

For NS crusts, the condition that DM crosses the non-degenerate layer is set by using the maximum ignition column depth at the carbon ocean in Ref. [76], which is about $\rho_{\text{env}} R_{\text{env}} \simeq 4 \times 10^{13} \text{ g} \cdot \text{cm}^{-2}$. The astrophysical constraints for Fermi-ball DM are shown in Fig. 1. The Fermi-ball fraction is set to be $f_X = 0.01$, and the results for $f_X = 1$ can be found in Supplementary Material. As more DM is focused, constraints are amplified when introducing the Yukawa interaction. The maximum value of DM mass to be constrained by WDs is $6.25 \times 10^{18} \text{ g}$ and $6.46 \times 10^{20} \text{ g}$ for $\tilde{\alpha} = 0$ and $\tilde{\alpha} = 100$, respectively.

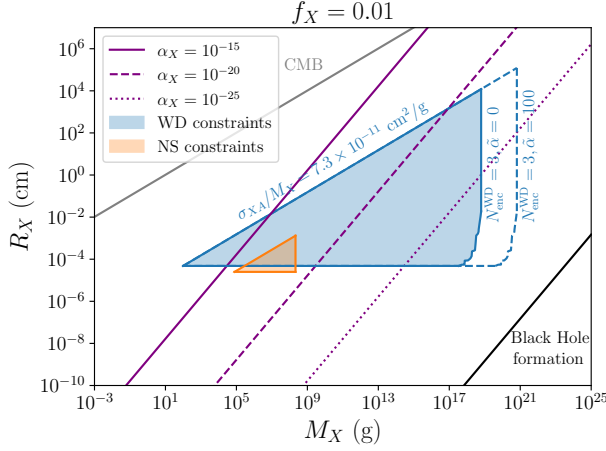


Figure 1. WD and NS constraints on Fermi-ball DM. The blue solid line represents the constraint with only gravitational interaction, and the dashed line represents the constraint with extra Yukawa attraction. The gray line represents the CMB constraints [8, 9].

For NS the value for $\tilde{\alpha} = 0$ is 2.14×10^8 g. The Fermi-ball will collapse into a black hole when its radius drops below the Schwarzschild radius $2GM_X$.

Signals at GW experiments.— As a macroscopic DM object passes near the detector, its gravitational influence causes differential acceleration among the test masses of GW detectors, producing a detectable Doppler signal. In the scenario where DM transits near a GW detection satellite, we assume the process occurs within the $x - y$ plane, with the DM moving along the y -direction at velocity v_{DM} . The resulting differential acceleration of the nearest interferometer node can be expressed as [42, 45]

$$\mathbf{g}(t) = \frac{\tilde{G}M_X}{D^2} \frac{1}{\left(1 + \left(\frac{v_{\text{DM}}t}{D}\right)^2\right)^{3/2}} \begin{pmatrix} 1 \\ \frac{v_{\text{DM}}t}{D} \\ 0 \end{pmatrix}, \quad (20)$$

where D is the impact factor of DM with respect to the nearest satellite and \tilde{G} is given by $G(1 + \tilde{\alpha})$ after taking into account the long-range Yukawa interaction. In the following, we use the SI units to make the results clearer. After integration, the velocity of the test mass induced by the trajectory of DM reads,

$$\mathbf{v}(t, D) = \frac{\tilde{G}M_X}{Dv_{\text{DM}}} \begin{bmatrix} 1 + \frac{v_{\text{DM}}t/D}{\sqrt{1 + v_{\text{DM}}^2 t^2/D^2}} \\ -\frac{1}{\sqrt{1 + v_{\text{DM}}^2 t^2/D^2}} \\ 0 \end{bmatrix}. \quad (21)$$

So in the limit $t \rightarrow -\infty$, the test mass is at rest. At $t \rightarrow \infty$, the velocity of the satellite approaches the x -direction and is equal to $\frac{2\tilde{G}M_X}{Dv_{\text{DM}}}$.

The DM interacts with three nodes of the detector simultaneously. We assume that the impact factor between

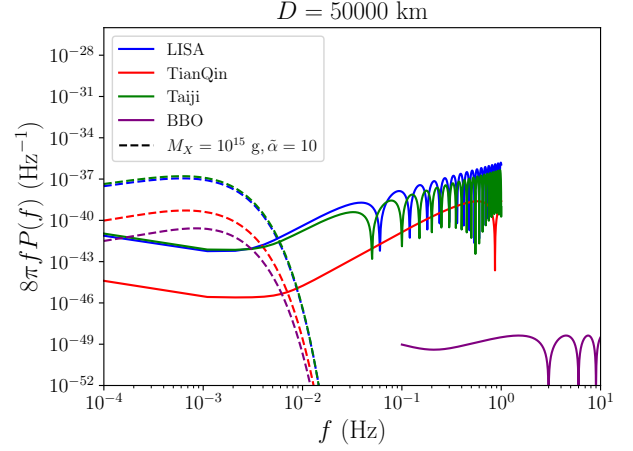


Figure 2. The signal PSD (dashed lines) of Fermi-ball DM on the GW detectors in the X channel and the corresponding noise PSD (solid lines).

the DM and the other two nodes is D' . We use U_i and V_i to encode the possible Doppler shifts of the laser beams that are exchanged between the detector nodes. In order to effectively cancel the laser noise, time-delay interferometry is employed [86–88]. For instance, the signal in Michelson-like X channel combination reads,

$$X(t) = U_1(t) + V_1(t) - U_1\left(t - \frac{2L}{c}\right) - V_1\left(t - \frac{2L}{c}\right) + U_2\left(t - \frac{3L}{c}\right) + V_3\left(t - \frac{3L}{c}\right) - U_2\left(t - \frac{L}{c}\right) - V_3\left(t - \frac{L}{c}\right) \quad (22)$$

with

$$U_1(t) = \mathbf{n}_2 \cdot \frac{\mathbf{v}_1(t) - \mathbf{v}_3(t - L/c)}{c}, \quad (23)$$

$$V_1(t) = \mathbf{n}_3 \cdot \frac{\mathbf{v}_1(t) - \mathbf{v}_2(t - L/c)}{c}, \quad (24)$$

and permutation symmetry $1 \rightarrow 2 \rightarrow 3 \rightarrow 1$. \mathbf{n}_i is defined as the unit vector between two nodes, labeled by the opposite side of the triangle, while \mathbf{v}_i refers to the corresponding velocity perturbation of the i -th node induced by gravitational pull. Note that $\mathbf{v}_1(t) = \mathbf{v}(t, D)$ and $\mathbf{v}_2(t) = \mathbf{v}_3(t) = \mathbf{v}(t, D')$. By using the relation $\mathbf{n}_2 + \mathbf{n}_3 = -\mathbf{n}_1$,

$$X(t) = -\mathbf{n}_1 \cdot \left[\frac{\mathbf{v}(t, D) - \mathbf{v}(t - 4L/c, D)}{c} + 2\frac{\mathbf{v}(t - 3L/c, D')}{c} - 2\frac{\mathbf{v}(t - L/c, D')}{c} \right]. \quad (25)$$

For arbitrary orientation of the detector plane relative to the DM, $\mathbf{n}_1 = (\sin \vartheta \cos \varphi, \sin \vartheta \sin \varphi, \cos \vartheta)$. For simplicity, we set $D' = D + L$ by taking into account

the larger distance with respect to the other two nodes due to the arm length. Some works consider the close approach limit, where the DM is restricted to passing by an interferometer node with an impact parameter smaller than the characteristic size of the detector, $D < L$ [42, 45]. The GW detector is moving through the halo at a constant velocity, and the DM velocity follows the Maxwell-Boltzmann distribution, $f(v_{\text{DM}}) = \frac{1}{\sqrt{2\pi\bar{v}^2}} \exp\left[-\frac{1}{2}\left(\frac{v_{\text{DM}} - v_{\odot}}{\bar{v}}\right)^2\right]$ where $\bar{v} = v_{\text{rms}}/\sqrt{3}$ with $v_{\text{rms}} \approx 270$ km/s [89]. As the DM speed is concentrated within a specific range, we set $v_{\text{DM}} \approx v_{\odot}$. Complete calculation needs Monte-Carlo simulation for the geometry of the detectors, DM position and DM velocity distribution. We leave this in our future work. Finally, the power spectral density (PSD) of the signal reads,

$$P(\omega) = \frac{1}{4\pi} \int d\cos\vartheta \int d\varphi \left| \tilde{X}(\omega) \right|^2. \quad (26)$$

where $\tilde{X}(\omega)$ is the Fourier transformation of $X(t)$ and $\omega = 2\pi f$. In Fig. 2 we show the DM signals and the corresponding noise PSD S_n for LISA [62], TianQin [63], Taiji [90], and BBO [91]. The complete formula for signal PSD in the three TDI channels and the corresponding noise PSD can be seen in the Supplementary Material.

We employ the X channel to derive our main result. The detectability of GW detectors is evaluated by the signal-to-noise ratio (SNR),

$$\text{SNR} = \left(4 \int_0^\infty d\omega \frac{P(\omega)}{S_n(\omega)} \right)^{\frac{1}{2}}. \quad (27)$$

In order to avoid the constraints of MICROSCOPE and the bullet cluster, f_X and δ_{SM} are set to be $f_X = 0.01$ and $\delta_{\text{SM}} = 10^{-6}$, respectively. The DM impacts on GW detectors are approximately a Poisson process. The corresponding probability is $(N_{\text{enc}}^{\text{GW}})^n e^{-N_{\text{enc}}^{\text{GW}}}/n!$ where n and $N_{\text{enc}}^{\text{GW}} = (f_X \pi D^2 \rho_{\text{DM}} v_{\text{DM}} / M_X) T_{\text{obs}}^i$ are the number of DM and the expected number of DM passing through the detector i , respectively. We restrict $N_{\text{enc}}^{\text{GW}} = 1$ so that at least one DM induced event will be expected during the lifetime T_{obs}^i of the experiments. The results of the sensitivity of the GW detectors after fixing $\text{SNR} \geq 10$ are shown in Fig. 3. GW detectors have the ability to detect DM with mass $1 - 10^{14}$ g and coupling $\alpha_X > 10^{-17}$. The detectability of GW detectors is strongest around $10^{11} - 10^{12}$ g. Below this value, the PSD of the signal is proportional to $\tilde{G}^2 M_X^2$, so α_X must be increased to compensate for the decrease in M_X . On the other hand, if the DM mass is too large, the impact factor D has to be increased for a fixed event rate. The signals suffer an extra exponential suppression, and then α_X needs to be increased again. The NS heating constraint due to the energy transfer from DM that is not gravitationally captured has been considered [70]. The sensitivity of GW

detectors on DM for $f_X = 1$ and expected events for a fixed SNR are shown in the Supplementary Material.

We also perform Fisher matrix analysis to forecast the precision of model parameters. The full analysis can be seen in the Supplementary Material. The marginalized $1-\sigma$ uncertainty on the i -th parameter is estimated as the square root of the diagonal element of the covariance matrix, which is the inverse of the Fisher matrix. For example, our results indicate that for $M_X = 10^8$ g, $\alpha_X = 10^{-13.5}$ and $D = 10$ km, the uncertainties are $\log_{10}(M_X/\text{g}) = 8.0 \pm 0.19$ and $\log_{10} \alpha_X = -13.5 \pm 0.23$ at TianQin, showing the superiority of GW detectors for DM detections.

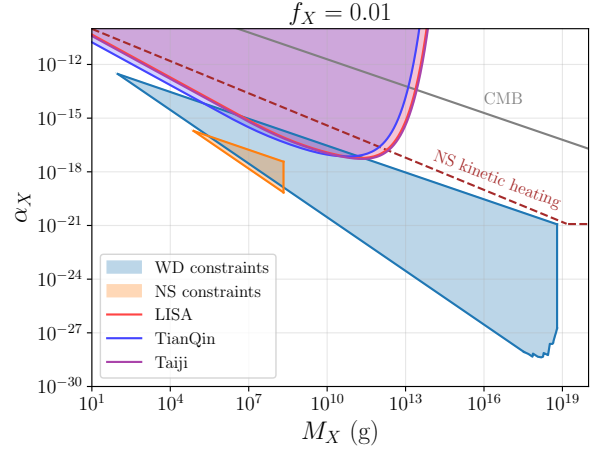


Figure 3. Projected sensitivity of GW detectors to Fermi-ball DM with updated astrophysical constraints. The brown line and the gray line denote the constraints from NS kinetic heating and CMB, respectively.

Conclusion— In this Letter, we have established a unified framework to constrain macroscopic DM, specifically Fermi-balls, by bridging the gap between astrophysical observations and precision interferometry. By adopting more rigorous analysis of white dwarf envelopes and incorporating expanded data, we derived a conservative bound of $\sigma_{XA}/M_X \gtrsim 7.3 \times 10^{-11} \text{ cm}^2/\text{g}$, which updates previous estimates by orders of magnitude.

Complementing astrophysical bounds, we demonstrated that space-borne GW observatories, such as LISA and TianQin, can serve as sensitive detector by monitoring the kinematic response of its test masses to passing DM. We found that they can identify sub-saturated Fermi-balls with masses spanning $1-10^{14}$ g and $\alpha_X \gtrsim 10^{-17}$. Furthermore, our Fisher analysis reveals that these experiments can achieve percent-level precision in parameter estimation, highlighting their ability to provide robust measurements.

Collectively, these results place macroscopic DM “under siege” from two directions. The combination of updated WD constraints and the novel use of GW inter-

ferometers as particle detectors offers a powerful, multi-messenger strategy to either discover or rule out a wide class of macroscopic candidates in the coming decade.

Acknowledgments— We would like to thank Yi-Ming Hu for the discussions on the sensitivity curves and Daneng Yang for discussions on the bullet cluster. This work is supported by the National Natural Science Foundation of China (NNSFC) under Grant No.12475111, No.12205387, and the Fundamental Research Funds for the Central Universities, Sun Yat-sen University.

* Corresponding Author. huangfp8@sysu.edu.cn

- [1] Alexander Kusenko, “Solitons in the supersymmetric extensions of the standard model,” *Phys. Lett. B* **405**, 108 (1997), [arXiv:hep-ph/9704273](#).
- [2] Alexander Kusenko and Mikhail E. Shaposhnikov, “Supersymmetric Q balls as dark matter,” *Phys. Lett. B* **418**, 46–54 (1998), [arXiv:hep-ph/9709492](#).
- [3] Edward Witten, “Cosmic Separation of Phases,” *Phys. Rev. D* **30**, 272–285 (1984).
- [4] E. Krylov, A. Levin, and V. Rubakov, “Cosmological phase transition, baryon asymmetry and dark matter Q-balls,” *Phys. Rev. D* **87**, 083528 (2013), [arXiv:1301.0354 \[hep-ph\]](#).
- [5] Fa Peng Huang and Chong Sheng Li, “Probing the baryogenesis and dark matter relaxed in phase transition by gravitational waves and colliders,” *Phys. Rev. D* **96**, 095028 (2017), [arXiv:1709.09691 \[hep-ph\]](#).
- [6] Jeong-Pyong Hong, Sunghoon Jung, and Ke-Pan Xie, “Fermi-ball dark matter from a first-order phase transition,” *Phys. Rev. D* **102**, 075028 (2020), [arXiv:2008.04430 \[hep-ph\]](#).
- [7] Siyu Jiang, Fa Peng Huang, and Pyungwon Ko, “Gauged Q-ball dark matter through a cosmological first-order phase transition,” *JHEP* **07**, 053 (2024), [arXiv:2404.16509 \[hep-ph\]](#).
- [8] David M. Jacobs, Glenn D. Starkman, and Bryan W. Lynn, “Macro Dark Matter,” *Mon. Not. Roy. Astron. Soc.* **450**, 3418–3430 (2015), [arXiv:1410.2236 \[astro-ph.CO\]](#).
- [9] Cora Dvorkin, Kfir Blum, and Marc Kamionkowski, “Constraining Dark Matter-Baryon Scattering with Linear Cosmology,” *Phys. Rev. D* **89**, 023519 (2014), [arXiv:1311.2937 \[astro-ph.CO\]](#).
- [10] Jagjit Singh Sidhu, Glenn Starkman, and Ralph Harvey, “Counter-top search for macroscopic dark matter,” *Phys. Rev. D* **100**, 103015 (2019), [arXiv:1905.10025 \[astro-ph.HE\]](#).
- [11] Jagjit Singh Sidhu and Glenn Starkman, “Macroscopic Dark Matter Constraints from Bolide Camera Networks,” *Phys. Rev. D* **100**, 123008 (2019), [arXiv:1908.00557 \[astro-ph.CO\]](#).
- [12] Leonardo Badurina, Yufeng Du, Vincent S. H. Lee, Yikun Wang, and Kathryn M. Zurek, “Detecting gravitational signatures of dark matter with atom gradiometers,” *Phys. Rev. D* **112**, 063014 (2025), [arXiv:2505.00781 \[hep-ph\]](#).
- [13] Yang Bai, Sida Lu, and Nicholas Orlofsky, “Gravitational waves from more attractive dark binaries,” *JCAP* **08**, 057 (2024), [arXiv:2312.13378 \[astro-ph.CO\]](#).
- [14] Digvijay Wadekar and Zihui Wang, “Constraining axion and compact dark matter with interstellar medium heating,” *Phys. Rev. D* **107**, 083011 (2023), [arXiv:2211.07668 \[hep-ph\]](#).
- [15] Peter W. Graham, Surjeet Rajendran, and Jaime Varela, “Dark Matter Triggers of Supernovae,” *Phys. Rev. D* **92**, 063007 (2015), [arXiv:1505.04444 \[hep-ph\]](#).
- [16] Peter W. Graham, Ryan Janish, Vijay Narayan, Surjeet Rajendran, and Paul Riggins, “White Dwarfs as Dark Matter Detectors,” *Phys. Rev. D* **98**, 115027 (2018), [arXiv:1805.07381 \[hep-ph\]](#).
- [17] Jagjit Singh Sidhu and Glenn D. Starkman, “Reconsidering astrophysical constraints on macroscopic dark matter,” *Phys. Rev. D* **101**, 083503 (2020), [arXiv:1912.04053 \[astro-ph.CO\]](#).
- [18] Nirmal Raj, “Supernovae and superbursts triggered by dark matter clumps,” *Phys. Rev. D* **109**, 123020 (2024), [arXiv:2306.14981 \[hep-ph\]](#).
- [19] Gianfranco Bertone and Malcolm Fairbairn, “Compact Stars as Dark Matter Probes,” *Phys. Rev. D* **77**, 043515 (2008), [arXiv:0709.1485 \[astro-ph\]](#).
- [20] Matthew McCullough and Malcolm Fairbairn, “Capture of Inelastic Dark Matter in White Dwarves,” *Phys. Rev. D* **81**, 083520 (2010), [arXiv:1001.2737 \[hep-ph\]](#).
- [21] Dan Hooper, Douglas Spolyar, Alberto Vallinotto, and Nickolay Y. Gnedin, “Inelastic Dark Matter As An Efficient Fuel For Compact Stars,” *Phys. Rev. D* **81**, 103531 (2010), [arXiv:1002.0005 \[hep-ph\]](#).
- [22] Bridget Bertoni, Ann E. Nelson, and Sanjay Reddy, “Dark Matter Thermalization in Neutron Stars,” *Phys. Rev. D* **88**, 123505 (2013), [arXiv:1309.1721 \[hep-ph\]](#).
- [23] Joseph Bramante, “Dark matter ignition of type Ia supernovae,” *Phys. Rev. Lett.* **115**, 141301 (2015), [arXiv:1505.07464 \[hep-ph\]](#).
- [24] Basudeb Dasgupta, Aritra Gupta, and Anupam Ray, “Dark matter capture in celestial objects: Improved treatment of multiple scattering and updated constraints from white dwarfs,” *JCAP* **08**, 018 (2019), [arXiv:1906.04204 \[hep-ph\]](#).
- [25] Nicole F. Bell, Giorgio Busoni, Sandra Robles, and Michael Virgato, “Improved Treatment of Dark Matter Capture in Neutron Stars,” *JCAP* **09**, 028 (2020), [arXiv:2004.14888 \[hep-ph\]](#).
- [26] Basudeb Dasgupta, Aritra Gupta, and Anupam Ray, “Dark matter capture in celestial objects: light mediators, self-interactions, and complementarity with direct detection,” *JCAP* **10**, 023 (2020), [arXiv:2006.10773 \[hep-ph\]](#).
- [27] Debajit Bose and Sambo Sarkar, “Impact of galactic distributions in celestial capture of dark matter,” *Phys. Rev. D* **107**, 063010 (2023), [arXiv:2211.16982 \[astro-ph.CO\]](#).
- [28] Thong T. Q. Nguyen and Tim M. P. Tait, “Bounds on long-lived dark matter mediators from neutron stars,” *Phys. Rev. D* **107**, 115016 (2023), [arXiv:2212.12547 \[hep-ph\]](#).
- [29] Liangliang Su, Lei Wu, and Meiwen Yang, “Deep inelastic scattering in the capture of dark matter by neutron stars,” *Phys. Rev. D* **110**, 055014 (2024), [arXiv:2408.03759 \[hep-ph\]](#).
- [30] Pooja Bhattacharjee, Sandra Robles, Stephan A. Meighen-Berger, and Francesca Calore, “Can local white dwarfs constrain dark matter interactions?” *JCAP* **10**, 093 (2025), [arXiv:2505.13629 \[hep-ph\]](#).

- [31] Samuel D. McDermott, Hai-Bo Yu, and Kathryn M. Zurek, “Constraints on Scalar Asymmetric Dark Matter from Black Hole Formation in Neutron Stars,” *Phys. Rev. D* **85**, 023519 (2012), [arXiv:1103.5472 \[hep-ph\]](#).
- [32] Chris Kouvaris and Peter Tinyakov, “Excluding Light Asymmetric Bosonic Dark Matter,” *Phys. Rev. Lett.* **107**, 091301 (2011), [arXiv:1104.0382 \[astro-ph.CO\]](#).
- [33] Joseph Bramante, Keita Fukushima, and Jason Kumar, “Constraints on bosonic dark matter from observation of old neutron stars,” *Phys. Rev. D* **87**, 055012 (2013), [arXiv:1301.0036 \[hep-ph\]](#).
- [34] Nicole F. Bell, Andrew Melatos, and Kalliopi Petraki, “Realistic neutron star constraints on bosonic asymmetric dark matter,” *Phys. Rev. D* **87**, 123507 (2013), [arXiv:1301.6811 \[hep-ph\]](#).
- [35] Ryan Janish, Vijay Narayan, and Paul Riggins, “Type Ia supernovae from dark matter core collapse,” *Phys. Rev. D* **100**, 035008 (2019), [arXiv:1905.00395 \[hep-ph\]](#).
- [36] Chih-Ting Lu, Arvind Kumar Mishra, and Lei Wu, “Constraining bosonic dark matter-baryon interactions from neutron star collapse,” *JCAP* **09**, 066 (2024), [arXiv:2404.07187 \[hep-ph\]](#).
- [37] Ning Liu and Arvind Kumar Mishra, “Neutron star collapse from accretion: A probe of massive dark matter particles,” *Phys. Dark Univ.* **47**, 101740 (2025), [arXiv:2408.00594 \[astro-ph.CO\]](#).
- [38] Arnaud de Lavallaz and Malcolm Fairbairn, “Neutron Stars as Dark Matter Probes,” *Phys. Rev. D* **81**, 123521 (2010), [arXiv:1004.0629 \[astro-ph.GA\]](#).
- [39] C. J. Horowitz, “Nuclear and dark matter heating in massive white dwarf stars,” *Phys. Rev. D* **102**, 083031 (2020), [arXiv:2008.03291 \[astro-ph.SR\]](#).
- [40] Yohei Ema, Robert McGehee, Maxim Pospelov, and Anupam Ray, “Dark matter catalyzed baryon destruction,” *Phys. Rev. D* **111**, 023005 (2025), [arXiv:2405.18472 \[hep-ph\]](#).
- [41] A. W. Adams and J. S. Bloom, “Direct detection of dark matter with space-based laser interferometers,” (2004), [arXiv:astro-ph/0405266 \[astro-ph\]](#).
- [42] J. Y. Vinet, “LISA and asteroids,” *Class. Quant. Grav.* **23**, 4939–4944 (2006).
- [43] Evan D. Hall, Rana X. Adhikari, Valery V. Frolov, Holger Müller, Maxim Pospelov, and Rana X Adhikari, “Laser Interferometers as Dark Matter Detectors,” *Phys. Rev. D* **98**, 083019 (2018), [arXiv:1605.01103 \[gr-qc\]](#).
- [44] H. Grote and Y. V. Stadnik, “Novel signatures of dark matter in laser-interferometric gravitational-wave detectors,” *Phys. Rev. Res.* **1**, 033187 (2019), [arXiv:1906.06193 \[astro-ph.IM\]](#).
- [45] Joerg Jaeckel, Sebastian Schenk, and Michael Spannowsky, “Probing dark matter clumps, strings and domain walls with gravitational wave detectors,” *Eur. Phys. J. C* **81**, 828 (2021), [arXiv:2004.13724 \[astro-ph.CO\]](#).
- [46] Valentin Thoss and Abraham Loeb, “Detecting dark objects in the Solar System with gravitational wave observatories,” *Phys. Rev. D* **112**, 083050 (2025), [arXiv:2507.19577 \[gr-qc\]](#).
- [47] Aaron Pierce, Keith Riles, and Yue Zhao, “Searching for Dark Photon Dark Matter with Gravitational Wave Detectors,” *Phys. Rev. Lett.* **121**, 061102 (2018), [arXiv:1801.10161 \[hep-ph\]](#).
- [48] Soichiro Morisaki and Teruaki Suyama, “Detectability of ultralight scalar field dark matter with gravitational-wave detectors,” *Phys. Rev. D* **100**, 123512 (2019), [arXiv:1811.05003 \[hep-ph\]](#).
- [49] Jiang-Chuan Yu, Yue-Hui Yao, Yong Tang, and Yue-Liang Wu, “Sensitivity of space-based gravitational-wave interferometers to ultralight bosonic fields and dark matter,” *Phys. Rev. D* **108**, 083007 (2023), [arXiv:2307.09197 \[gr-qc\]](#).
- [50] Yue-Hui Yao, Tingyuan Jiang, and Yong Tang, “Prospects for axion dark matter searches at LISA-like interferometers,” *Phys. Rev. D* **111**, 055031 (2025), [arXiv:2410.22072 \[hep-ph\]](#).
- [51] Jordan Gué, Aurélien Hees, and Peter Wolf, “Probing the axion–photon coupling with space-based gravitational wave detectors,” *Class. Quant. Grav.* **42**, 055015 (2025), [arXiv:2410.17763 \[hep-ph\]](#).
- [52] Run-Min Yao, Xiao-Jun Bi, Peng-Fei Yin, and Qing-Guo Huang, “Axion-like dark matter search with space-based gravitational wave detectors,” (2025), [arXiv:2504.10083 \[hep-ph\]](#).
- [53] Heng-Tao Xu, Yue-Hui Yao, Yong Tang, and Yue-Liang Wu, “Distinguishing monochromatic signals in lisa and taiji: Ultralight dark matter versus gravitational waves,” (2025), [arXiv:2506.09744 \[hep-ph\]](#).
- [54] Jordan Gué, Peter Wolf, and Aurélien Hees, “Discriminating scalar ultralight dark matter from quasi-monochromatic gravitational waves in lisa,” (2025), [arXiv:2508.13847 \[gr-qc\]](#).
- [55] Andrew L. Miller, “Gravitational wave probes of particle dark matter: a review,” (2025), [arXiv:2503.02607 \[astro-ph.HE\]](#).
- [56] Ethan R. Siegel, M. P. Hertzberg, and J. N. Fry, “Probing Dark Matter Substructure with Pulsar Timing,” *Mon. Not. Roy. Astron. Soc.* **382**, 879 (2007), [arXiv:astro-ph/0702546](#).
- [57] Shant Baghram, Niayesh Afshordi, and Kathryn M. Zurek, “Prospects for Detecting Dark Matter Halo Substructure with Pulsar Timing,” *Phys. Rev. D* **84**, 043511 (2011), [arXiv:1101.5487 \[astro-ph.CO\]](#).
- [58] Vincent S. H. Lee, Andrea Mitridate, Tanner Trickle, and Kathryn M. Zurek, “Probing Small-Scale Power Spectra with Pulsar Timing Arrays,” *JHEP* **06**, 028 (2021), [arXiv:2012.09857 \[astro-ph.CO\]](#).
- [59] Vincent S. H. Lee, Stephen R. Taylor, Tanner Trickle, and Kathryn M. Zurek, “Bayesian Forecasts for Dark Matter Substructure Searches with Mock Pulsar Timing Data,” *JCAP* **08**, 025 (2021), [arXiv:2104.05717 \[astro-ph.CO\]](#).
- [60] Harikrishnan Ramani, Tanner Trickle, and Kathryn M. Zurek, “Observability of Dark Matter Substructure with Pulsar Timing Correlations,” *JCAP* **12**, 033 (2020), [arXiv:2005.03030 \[astro-ph.CO\]](#).
- [61] Yufeng Du, Vincent S. H. Lee, Yikun Wang, and Kathryn M. Zurek, “Macroscopic dark matter detection with gravitational wave experiments,” *Phys. Rev. D* **108**, 122003 (2023), [arXiv:2306.13122 \[astro-ph.CO\]](#).
- [62] Pau Amaro-Seoane *et al.*, “Laser interferometer space antenna,” (2017), [arXiv:1702.00786 \[astro-ph.IM\]](#).
- [63] Jun Luo *et al.* (TianQin), “TianQin: a space-borne gravitational wave detector,” *Class. Quant. Grav.* **33**, 035010 (2016), [arXiv:1512.02076 \[astro-ph.IM\]](#).
- [64] Moira I. Gresham, Hou Keong Lou, and Kathryn M. Zurek, “Nuclear Structure of Bound States of Asymmetric Dark Matter,” *Phys. Rev. D* **96**, 096012 (2017), [arXiv:1707.02313 \[hep-ph\]](#).
- [65] Joel Bergé, Philippe Brax, Gilles Métris, Martin Pernot-

- Borràs, Pierre Touboul, and Jean-Philippe Uzan, “MICROSCOPE Mission: First Constraints on the Violation of the Weak Equivalence Principle by a Light Scalar Dilaton,” *Phys. Rev. Lett.* **120**, 141101 (2018), [arXiv:1712.00483 \[gr-qc\]](#).
- [66] Pierre Fayet, “MICROSCOPE limits on the strength of a new force, with comparisons to gravity and electromagnetism,” *Phys. Rev. D* **99**, 055043 (2019), [arXiv:1809.04991 \[hep-ph\]](#).
- [67] David N. Spergel and Paul J. Steinhardt, “Observational evidence for selfinteracting cold dark matter,” *Phys. Rev. Lett.* **84**, 3760–3763 (2000), [arXiv:astro-ph/9909386](#).
- [68] Felix Kahlhoefer, Kai Schmidt-Hoberg, Mads T. Frandsen, and Subir Sarkar, “Colliding clusters and dark matter self-interactions,” *Mon. Not. Roy. Astron. Soc.* **437**, 2865–2881 (2014), [arXiv:1308.3419 \[astro-ph.CO\]](#).
- [69] David Harvey, Richard Massey, Thomas Kitching, Andy Taylor, and Eric Tittley, “The non-gravitational interactions of dark matter in colliding galaxy clusters,” *Science* **347**, 1462–1465 (2015), [arXiv:1503.07675 \[astro-ph.CO\]](#).
- [70] Moira I. Gresham, Vincent S. H. Lee, and Kathryn M. Zurek, “Astrophysical observations of a dark matter-Baryon fifth force,” *JCAP* **02**, 048 (2023), [arXiv:2209.03963 \[astro-ph.HE\]](#).
- [71] F. X. Timmes and S. E. Woosley, “The Conductive Propagation of Nuclear Flames. I. Degenerate C + O and O + NE + MG White Dwarfs,” *ApJ* **396**, 649 (1992).
- [72] Michael A. Fedderke, Peter W. Graham, and Surjeet Rajendran, “White dwarf bounds on charged massive particles,” *Phys. Rev. D* **101**, 115021 (2020), [arXiv:1911.08883 \[hep-ph\]](#).
- [73] Richard C. Tolman, “Static solutions of Einstein’s field equations for spheres of fluid,” *Phys. Rev.* **55**, 364–373 (1939).
- [74] J. R. Oppenheimer and G. M. Volkoff, “On massive neutron cores,” *Phys. Rev.* **55**, 374–381 (1939).
- [75] P. Dufour, S. Blouin, S. Coutu, M. Fortin-Archambault, C. Thibeault, P. Bergeron, and G. Fontaine, “The montreal white dwarf database: a tool for the community,” (2016), [arXiv:1610.00986 \[astro-ph.SR\]](#).
- [76] Andrew Cumming and Lars Bildsten, “Carbon flashes in the heavy element ocean on accreting neutron stars,” *Astrophys. J. Lett.* **559**, L127 (2001), [arXiv:astro-ph/0107213](#).
- [77] Tolga Guver, Patricia Wroblewski, Larry Camarota, and Feryal Özel, “The Mass and Radius of the Neutron Star in 4U 1820-30,” *Astrophys. J.* **719**, 1807 (2010), [arXiv:1002.3825 \[astro-ph.HE\]](#).
- [78] B. Datta, A. V. Thampan, and D. Bhattacharya, “A Numerical Survey of Neutron Star Crustal Density Profiles,” *Journal of Astrophysics and Astronomy* **16**, 375 (1995).
- [79] F. J. Kerr and D. Lynden-Bell, “Review of galactic constants,” *Monthly Notices of the Royal Astronomical Society* **221**, 1023–1038 (1986).
- [80] A. K. Drukier, Katherine Freese, and D. N. Spergel, “Detecting Cold Dark Matter Candidates,” *Phys. Rev. D* **33**, 3495–3508 (1986).
- [81] Joss Bland-Hawthorn and Ortwin Gerhard, “The Galaxy in Context: Structural, Kinematic, and Integrated Properties,” *Ann. Rev. Astron. Astrophys.* **54**, 529–596 (2016), [arXiv:1602.07702 \[astro-ph.GA\]](#).
- [82] N. Wyn Evans, Ciaran A. J. O’Hare, and Christopher McCabe, “Refinement of the standard halo model for dark matter searches in light of the Gaia Sausage,” *Phys. Rev. D* **99**, 023012 (2019), [arXiv:1810.11468 \[astro-ph.GA\]](#).
- [83] Julio F. Navarro, Carlos S. Frenk, and Simon D. M. White, “A Universal density profile from hierarchical clustering,” *Astrophys. J.* **490**, 493–508 (1997), [arXiv:astro-ph/9611107](#).
- [84] Kensuke Akita, Gaetano Lambiase, Michiru Niibo, and Masahide Yamaguchi, “Neutrino lines from MeV dark matter annihilation and decay in JUNO,” *JCAP* **10**, 097 (2022), [arXiv:2206.06755 \[hep-ph\]](#).
- [85] S. L. Shapiro and S. A. Teukolsky, *Black holes, white dwarfs, and neutron stars: The physics of compact objects* (1983).
- [86] J. W. Armstrong, F. B. Estabrook, and Massimo Tinto, “Time-delay interferometry for space-based gravitational wave searches,” *The Astrophysical Journal* **527**, 814 (1999).
- [87] S. V. Dhurandhar, K. Rajesh Nayak, and J. Y. Vinet, “Algebraic approach to time-delay data analysis for LISA,” *Phys. Rev. D* **65**, 102002 (2002), [arXiv:gr-qc/0112059](#).
- [88] Massimo Tinto and Sanjeev V. Dhurandhar, “Time-delay interferometry,” *Living Rev. Rel.* **24**, 1 (2021).
- [89] Marc Kamionkowski and Ali Kinkhabwala, “Galactic halo models and particle dark matter detection,” *Phys. Rev. D* **57**, 3256–3263 (1998), [arXiv:hep-ph/9710337](#).
- [90] Wen-Rui Hu and Yue-Liang Wu, “The Taiji Program in Space for gravitational wave physics and the nature of gravity,” *Natl. Sci. Rev.* **4**, 685–686 (2017).
- [91] Vincent Corbin and Neil J. Cornish, “Detecting the cosmic gravitational wave background with the big bang observer,” *Class. Quant. Grav.* **23**, 2435–2446 (2006), [arXiv:gr-qc/0512039](#).
- [92] Alexei Yu. Smirnov and Xun-Jie Xu, “Neutrino bound states and bound systems,” *JHEP* **08**, 170 (2022), [arXiv:2201.00939 \[hep-ph\]](#).
- [93] Mark B. Wise and Yue Zhang, “Stable Bound States of Asymmetric Dark Matter,” *Phys. Rev. D* **90**, 055030 (2014), [Erratum: *Phys. Rev. D* **91**, 039907 (2015)], [arXiv:1407.4121 \[hep-ph\]](#).
- [94] Olaf Hartwig, Marc Lilley, Martina Muratore, and Mauro Pieroni, “Stochastic gravitational wave background reconstruction for a nonequilateral and unequal-noise LISA constellation,” *Phys. Rev. D* **107**, 123531 (2023), [arXiv:2303.15929 \[gr-qc\]](#).
- [95] Stanislav Babak, Martin Hewitson, and Antoine Petiteau, “Lisa sensitivity and snr calculations,” (2021), [arXiv:2108.01167 \[astro-ph.IM\]](#).
- [96] Raphael Flauger, Nikolaos Karnesis, Germano Nardini, Mauro Pieroni, Angelo Ricciardone, and Jesús Torrado, “Improved reconstruction of a stochastic gravitational wave background with LISA,” *JCAP* **01**, 059 (2021), [arXiv:2009.11845 \[astro-ph.CO\]](#).
- [97] Djuna Croon, David McKeen, Nirmal Raj, and Zihui Wang, “Subaru-HSC through a different lens: Microlensing by extended dark matter structures,” *Phys. Rev. D* **102**, 083021 (2020), [arXiv:2007.12697 \[astro-ph.CO\]](#).
- [98] Hiroko Niikura *et al.*, “Microlensing constraints on primordial black holes with Subaru/HSC Andromeda observations,” *Nature Astron.* **3**, 524–534 (2019), [arXiv:1701.02151 \[astro-ph.CO\]](#).

Supplementary Material

Siyu Jiang, Aidi Yang, Fa Peng Huang

CONTENTS

I. Fermi-ball Profile Computation	1
I.a. Derivations of $\langle \bar{X}X \rangle$ and $\langle X^\dagger X \rangle$	1
I.b. Numerical solutions	2
I.c. Analytical evaluations	3
II. Some details about the astrophysical constraints	4
II.a. The heat capacity for different particle species	4
II.b. Maximum impact factor	4
II.c. The width of a non-degenerate WD envelope	5
III. More details on the signals induced by DM in GW detectors	6
III.a. Signal and noise PSD for X , α and ζ combinations	6
III.b. Expected number of DM passes through the detectors for fixed SNR	8
III.c. The sensitivity of GW detectors on DM in sight of astrophysical constraints for $f_X = 1$	8
III.d. Full Fisher matrix analysis	10

I. FERMI-BALL PROFILE COMPUTATION

I.a. Derivations of $\langle \bar{X}X \rangle$ and $\langle X^\dagger X \rangle$

We briefly give the derivation of Eqs. (10) and (11). More details can be found in Ref. [92]. Consider a single particle state,

$$X_i(\mathbf{x}) \equiv \int \frac{d^3\mathbf{k}}{(2\pi)^3} \frac{w_i(\mathbf{k})}{\sqrt{2E_k}} u^s(k) e^{i\mathbf{k}\cdot\mathbf{x}}. \quad (1)$$

where w_i is the wave-packet function, and the spinor u^s satisfies

$$u^{s\dagger}(k)u^s(k) = 2E_k, \quad \overline{u^s(k)}u^s(k) = 2m_X. \quad (2)$$

Then the average of $X^\dagger X$ in the total system of N particles,

$$\begin{aligned} \langle X^\dagger X \rangle &= \sum_{i=1}^N \frac{1}{\Delta x^3} \int_{-\infty}^{+\infty} d^3\mathbf{x} X^\dagger(\mathbf{x}) X(\mathbf{x}) \\ &= \sum_{i=1}^N \frac{1}{\Delta x^3} \int \frac{d^3\mathbf{k}}{(2\pi)^3} \frac{d^3\mathbf{p}}{(2\pi)^3} \frac{u^{s\dagger}(k)u^s(p)}{\sqrt{2E_k}\sqrt{2E_p}} w_i^*(\mathbf{k}) w_i(\mathbf{p}) \times \left[\int_{-\infty}^{+\infty} d^3\mathbf{x} e^{i(\mathbf{p}-\mathbf{k})\cdot\mathbf{x}} \right] \\ &= \sum_{i=1}^N \frac{1}{\Delta x^3} \int \frac{d^3\mathbf{k}}{(2\pi)^3} \frac{u^{s\dagger}(k)u^s(k)}{2E_k} |w_i(\mathbf{k})|^2. \end{aligned} \quad (3)$$

Recall the definition of the distribution function,

$$f(\mathbf{k}) = \frac{1}{\Delta x^3} \sum_{i=1}^N |w_i(\mathbf{k})|^2, \quad (4)$$

we get

$$\langle X^\dagger X \rangle = \int \frac{d^3\mathbf{k}}{(2\pi)^3} f(\mathbf{k}). \quad (5)$$

And similarly for $\langle \bar{X} X \rangle$,

$$\langle \bar{X} X \rangle = \int \frac{d^3 \mathbf{k}}{(2\pi)^3} \frac{m_X}{E_k} f(\mathbf{k}) . \quad (6)$$

In the limit of zero temperature,

$$f = \frac{1}{e^{(E-\mu)/T} + 1} \approx \Theta(\mu - E) = \Theta(k_F - k) . \quad (7)$$

I.b. Numerical solutions

The equation of motion of X and ϕ can be derived from Eq. (1),

$$[i\partial - (m_X - y_X \phi(\mathbf{r}))] X(x) = 0 , \quad (8)$$

$$\nabla^2 \phi - m_\phi^2 \phi + y_X \langle \bar{X} X \rangle = 0 , \quad (9)$$

where

$$\langle \bar{X} X \rangle = \frac{g_X}{2\pi^2} \int_0^{k_F(\phi)} dk \frac{k^2 (m_X - y_X \phi)}{\sqrt{k^2 + (m_X - y_X \phi)^2}} , \quad (10)$$

$$\langle X^\dagger X \rangle = \frac{g_X}{2\pi^2} \int_0^{k_F(\phi)} dk k^2 = \frac{g_X}{6\pi^2} k_F(\phi)^3 , \quad (11)$$

with g_X and k_F being the degree of freedom and the Fermi momentum, respectively. We will assume the Fermi-ball is spherical. Out of the Fermi-ball, $r > R_X$, the equation of motion can be solved analytically, $\phi(r) \simeq \phi(R_X) e^{-m_\phi(r-R_X)} R_X/r$. So, the boundary conditions are as follows,

$$\partial_r \phi(0) = 0, \quad \phi(R_X) = \frac{m_X - \mu}{y_X}, \quad \partial_r \phi(R_X) = \frac{(\mu - m_X)}{y_X} \frac{1 + m_\phi R_X}{R_X} . \quad (12)$$

For the numerical solution of the Fermi-ball profile, it is convenient to rewrite the equation of motion of ϕ in Eq. (9) in terms of $f(r) = (m_X - y_X \phi(r)) / \mu$. And by using the definition $\tilde{m}_X = m_X / \mu$, $\tilde{m}_\phi = m_\phi / \mu$, $\rho = \mu r$, then Eq. (9) reads as follows

$$\frac{1}{\rho} \frac{d^2}{d\rho^2} (\rho f) = -\tilde{m}_\phi^2 (\tilde{m}_X - f) + \frac{\alpha_X g_X}{\pi} \left[f \sqrt{1 - f^2} + f^3 \log \left(\frac{f}{1 + \sqrt{1 - f^2}} \right) \right] , \quad (13)$$

where $\alpha_X = y_X^2 / 4\pi$. The $f(\rho)$ subjects to the boundary conditions $f'(0) = 0$, $f(R_X) = 1$ and $f'(R_X) = (1 + m_\phi R_X)(m_X - \mu) / (\mu R_X)$. When the number of constituents N_X is large enough, $f - f(0)$ is exponentially small, resulting in very large numerical inaccuracies. In order to solve the problem, we adopt the method of Ref. [64]. Because $f - f(0)$ is exponentially small, the right side of Eq. (13) can be Taylor expanded,

$$\frac{d^2}{d\rho^2} (\rho f) \simeq \rho [\kappa^2 (f - f_0)] \quad (14)$$

with

$$\kappa^2 = \tilde{m}_\phi^2 + \frac{g_X \alpha_X}{\pi} \left[\sqrt{1 - f_0^2} + 3f_0^2 \log \left(\frac{f_0}{1 + \sqrt{1 - f_0^2}} \right) \right] . \quad (15)$$

The Eq. (14) can be easily solved,

$$f(\rho) \simeq f_0 + \frac{[f(0) - f_0] \sinh(\kappa \rho)}{\kappa \rho} . \quad (16)$$

The boundary condition can then be replaced by the value at some intermediate point $\rho = \rho_0$, where ρ_0 is of the order $1/\kappa$. Then we integrate until R_X where $f(R_X) = 1$ and check if $f'(R_X)$ satisfies the boundary condition. The numerical profile can be easily obtained by using the overshooting-undershooting method. In Fig. 1 we show the DM radius versus N_X for $m_\phi/m_X = 10^{-4}$ and $m_\phi/m_X = 0$ respectively. The α_X is fixed to be 10^{-4} .

I.c. Analytical evaluations

We can also give some insights into the Fermi-balls analytically.

In the case of small N_X the nugget is small enough that $R_X \ll m_\phi^{-1}$, the constituents of Fermi-balls are largely non-relativistic and the effective mass $m_X - y_X \phi \approx m_X$. From the non-relativistic theory of fermi gas, the Fermi-ball has the behavior $N_X = \frac{81\pi^2}{4g_X^2 \alpha_X m_X^3 R_X^3}$ [93].

In the case of medium N_X , one can rewrite the equation of motion (13) as [64],

$$\frac{d}{dr} \left[\frac{1}{2} f'^2 - h(f) + m_\phi^2 \left(\frac{m_X}{\mu} f - \frac{1}{2} f^2 \right) \right] = \frac{2}{r} f'^2 \quad (17)$$

with

$$h(f) = 4\pi\alpha_X \mu^2 \int_0^f \psi(y) dy, \quad (18)$$

and

$$\psi(y) = \frac{g_X}{2\pi^2} \int_0^{\sqrt{1-y^2}} \frac{y k^2 dk}{\sqrt{k^2 + y^2}}. \quad (19)$$

In the medium N_X regime, where $m_\phi \sim 0$, $f(0) \sim 0$, and $\mu \ll m_X$, we obtain the relation,

$$\frac{1}{2} \left(\frac{m_X}{\mu R_X} \right)^2 \simeq 4\pi\alpha_X \mu^2 \int_0^1 \psi(y) dy = \frac{g_X \alpha_X \mu^2}{6\pi}. \quad (20)$$

By using $N_X \simeq \frac{2g_X}{9\pi} R_X^3 k_F^3(0) \simeq \frac{2g_X}{9\pi} R_X^3 \mu^3$, one can obtain

$$N_X = \frac{2g_X}{9\pi} \left(\frac{3\pi m_X^2}{g_X \alpha_X} \right)^{3/4} R_X^{3/2}, \quad (21)$$

and

$$M_X = N_X \mu = \frac{2}{3} \frac{m_X^2}{\alpha_X} R_X. \quad (22)$$

It can be seen that this analytical behavior is consistent with the numerical results in Fig. 1.

In contrast to the case of small N_X , when N_X is large enough, the Fermi-ball radius R_X becomes much larger than m_ϕ^{-1} . The effective mass approaches a constant, $m_X - y_X \phi(r) \rightarrow 0$ for $r < R_X$. The Fermi-ball is in saturation, the scalar field, effective mass, and the Fermi momentum are nearly constant inside the Fermi-ball, then from Eq. (2),

$$M_X \equiv E_X = \frac{4\pi}{3} R_X^3 \frac{m_\phi^2}{2} \frac{m_X^2}{y_X^2} + \frac{g_{\text{dof}}}{6\pi} \frac{N_X^{4/3}}{R_X} \left(\frac{9\pi^2}{2g_X} \right)^{4/3}. \quad (23)$$

By minimizing E_X with respect to the Fermi-ball radius, i.e., $dE_X/dR_X = 0$, we have

$$R_X = \frac{(3\pi)^{5/12} \alpha_X^{1/4}}{2^{1/3} g_X^{1/12} (m_X m_\phi)^{1/2}} N_X^{1/3}, \quad (24)$$

and

$$M_X = \frac{3^{1/4} \pi^{5/4} (m_X m_\phi)^{1/2}}{g_X^{1/4} \alpha_X^{1/4}} N_X. \quad (25)$$

The behaviors are also consistent with the numerical results in Fig. 1.

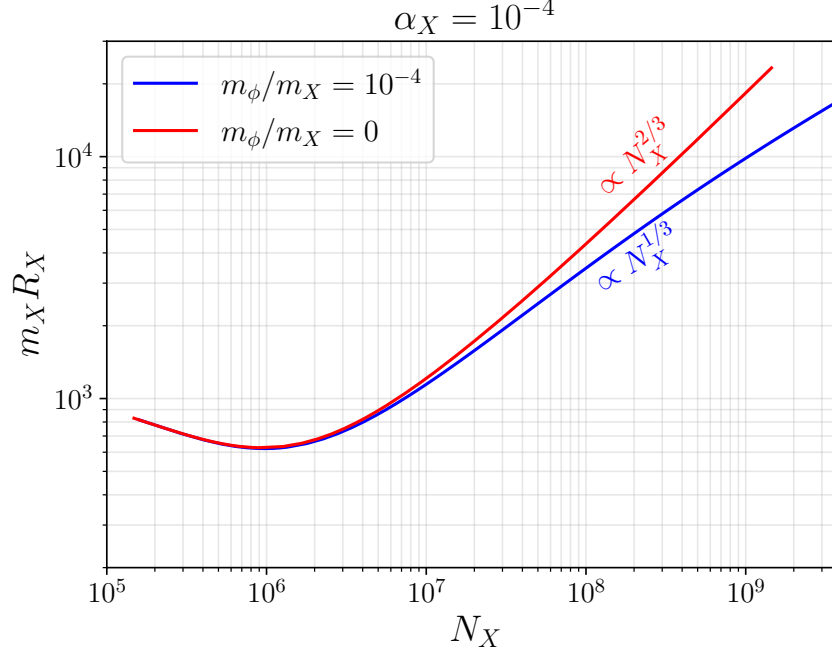


Figure 1. DM radius versus N_X for $\alpha_X = 10^{-4}$.

II. SOME DETAILS ABOUT THE ASTROPHYSICAL CONSTRAINTS

II.a. The heat capacity for different particle species

The heat capacity for ions, electrons, and photons is given by [72],

$$c_p^{\text{ion}}(T, \rho) \equiv \frac{5}{2\mu_a} \sum_i \frac{X_i}{A_i}, \quad (26)$$

$$c_p^e(T, \rho) \equiv \frac{\pi^2}{\mu_a \mu_e} \frac{T}{E_F} \left[1 - \left(\frac{m_e}{E_F} \right)^2 \right]^{-1}, \quad (27)$$

$$c_p^\gamma(T, \rho) \equiv \frac{4\pi^4}{5\mu_a \mu_e} \left(\frac{T}{E_F} \right)^3 \left[1 - \left(\frac{m_e}{E_F} \right)^2 \right]^{-3/2}, \quad (28)$$

where μ_a is the atomic mass unit. $\mu_e \equiv (\sum_i X_i Z_i / A_i)^{-1}$ is the mean molecular mass per electron with X_i, Z_i , and A_i being the mass fraction, charge, and atomic mass number of ion species i , respectively. For WDs we assume $X_C = X_O = 1/2$. $E_F = [1 + (3\pi^2 n_e / m_e^3)^{2/3}]^{1/2}$ is the electron Fermi energy and $n_e = \rho / (\mu_a \mu_e)$ is the electron number density.

II.b. Maximum impact factor

Throughout the DM trajectory, it satisfies the constraint $p_\mu p^\mu = M_X^2$. For a DM with energy $E = \gamma M_X = M_X / \sqrt{1 - v_{\text{DM}}^2}$, velocity v_{DM} , conserved angular momentum $L = \gamma M_X b v_{\text{DM}}$ with b being the impact factor, we get the following relation [70],

$$\left(\frac{dr}{d\tau} \right)^2 = \left(\frac{E - V_{\text{eff},+}}{M_X} \right) \left(\frac{E - V_{\text{eff},-}}{M_X} \right) \quad (29)$$

with

$$\frac{V_{\text{eff},\pm}}{M_X} = -\frac{GM_{\text{CO}}\tilde{\alpha}e^{-m_\phi r}}{r} \pm \sqrt{\left(1 - \frac{2GM_{\text{CO}}}{r}\right)\left(\frac{(L/M_X)^2}{r^2} + 1\right)}, \quad (30)$$

where $\tilde{\alpha} = \delta_n \delta_X$. The maximum impact factor can be found by using the following conditions [70]

$$V'_{\text{eff},+}(r_b)|_{L=\gamma M_X b v_{\text{DM}}} = 0, \quad V_{\text{eff},+}(r_b)|_{L=\gamma M_X b v_{\text{DM}}} = \gamma M_X. \quad (31)$$

Using $v_{\text{DM}}^2 \ll \frac{GM}{R_{\text{CO}}} \ll 1$ and $\lambda \gg R_{\text{CO}}$, a good analytic approximation for b_{max} is given by the minimum of

$$b_{\text{max, in}} \approx \frac{R_{\text{CO}}}{v_{\text{DM}}} \sqrt{\frac{\frac{2GM_{\text{CO}}}{R_{\text{CO}}}(1 + \tilde{\alpha}e^{-R_{\text{CO}}/\lambda}) + \left(\frac{GM_{\text{CO}}}{R_{\text{CO}}}\tilde{\alpha}e^{-R_{\text{CO}}/\lambda}\right)^2}{\left(1 - \frac{2GM_{\text{CO}}}{R_{\text{CO}}}\right)}}, \quad (32)$$

and

$$b_{\text{max, out}} \approx \sqrt{\lambda x \left(\frac{2GM_{\text{CO}}}{v_{\text{DM}}^2} + \lambda x\right)}, \quad x \approx \log\left(\frac{\tilde{\alpha}}{\frac{\lambda v_{\text{DM}}^2}{GM_{\text{CO}}} + \frac{1}{\log \tilde{\alpha}}}\right), \quad (33)$$

so [70]

$$b_{\text{max}} = \min(b_{\text{max, in}}, b_{\text{max, out}}). \quad (34)$$

In the limit $\lambda \gg R_{\text{CO}}$,

$$b_{\text{max, in}} \approx \frac{R_{\text{CO}}}{v_{\text{DM}}} \sqrt{\frac{\frac{2GM_{\text{CO}}}{R_{\text{CO}}}(1 + \tilde{\alpha}) + \left(\frac{GM_{\text{CO}}}{R_{\text{CO}}}\tilde{\alpha}\right)^2}{\left(1 - \frac{2GM_{\text{CO}}}{R_{\text{CO}}}\right)}}. \quad (35)$$

When $\tilde{\alpha} \rightarrow 0$, the maximum impact factor is

$$b_{\text{max}} = \frac{R_{\text{CO}}}{v_{\text{DM}}} \sqrt{\frac{v_{\text{esc}}^2}{1 - v_{\text{esc}}^2}}, \quad (36)$$

which reproduces the formula without Yukawa interaction.

II.c. The width of a non-degenerate WD envelope

The density ρ_* and the temperature T_* at the transition point can be derived by equating the electron pressure of the degenerate layer to that of the non-degenerate layer [85],

$$\frac{\rho_* k T_*}{\mu_e \mu_a} = 1.0 \times 10^{13} \left(\frac{\rho_*}{\mu_e}\right)^{5/3}, \quad (37)$$

from which one get,

$$\rho_* = (2.4 \times 10^{-8} \text{ g} \cdot \text{cm}^{-3}) \mu_e T_*^{3/2}. \quad (38)$$

The photon diffusion equation is $L = -4\pi r^2 \frac{c}{3\kappa\rho} \frac{d}{dr}(aT^4)$ with a being the radiation constant and L_{WD} the luminosity. κ is the opacity of the stellar material and can be approximated by Kramer's opacity $\kappa = \kappa_0 \rho T^{-3.5}$ with

$$\kappa_0 = 4.34 \times 10^{24} Z(1+X) \text{ cm}^2 \cdot \text{g}^{-1}. \quad (39)$$

where X is the mass fraction of hydrogen and Z is the mass fraction of heavy elements other than hydrogen and helium. The photon diffusion equation gives,

$$\frac{dT}{dr} = -\frac{3}{4ac} \frac{\kappa \rho}{T^3} \frac{L}{4\pi r^2}. \quad (40)$$

By combining the photon diffusion equation and the equation of hydrostatic equilibrium $\frac{dP}{dr} = -\frac{GM_{\text{WD}}\rho}{r^2}$, the pressure P follows the following equation [85],

$$PdP = \frac{4ac}{3} \frac{4\pi GM_{\text{WD}}}{\kappa_0 L_{\text{WD}}} \frac{k}{\bar{\mu}\mu_a} T^{7.5} dT. \quad (41)$$

After integration and replacing P by ρ from the equation of state,

$$\rho = \left(\frac{8ac}{25.5} \frac{4\pi GM_{\text{WD}}}{\kappa_0 L_{\text{WD}}} \frac{\bar{\mu}\mu_a}{k} \right)^{1/2} T^{3.25}. \quad (42)$$

In terms of the luminosity L_{WD} by combining Eqs. (38) and (42), T_* can be expressed as,

$$L_{\text{WD}} = (5.7 \times 10^5 \text{ erg} \cdot \text{s}^{-1}) \times \frac{\bar{\mu}}{\mu_e^2} \frac{1}{Z(1+X)} \frac{M_{\text{WD}}}{M_{\odot}} \left(\frac{T_*}{1 \text{ K}} \right)^{3.5}, \quad (43)$$

where $\bar{\mu} \equiv (\sum_i X_i(1+Z_i)/A_i)^{-1}$ is the mean molecular weight. For WDs, L_{WD} can be derived from the cooling rate of the total thermal energy [85],

$$L_{\text{WD}} \approx (3.14 \times 10^{24} \text{ erg} \cdot \text{s}^{-1}) \times \left(\frac{1}{\bar{\mu}} - \frac{1}{\mu_e} \right) \left(\frac{M_{\text{WD}}}{M_{\odot}} \right) \left(\frac{1 \text{ Gyr}}{\tau_{\text{WD}}} \right) \left(\frac{T_*}{1 \text{ K}} \right). \quad (44)$$

Equate this to Eq. (43) we get

$$\left(\frac{T_*}{1 \text{ K}} \right)^{2.5} \simeq 5.5 \times 10^{18} Z(1+X) \frac{\mu_e}{\bar{\mu}} \left(\frac{\mu_e}{\bar{\mu}} - 1 \right) \left(\frac{1 \text{ Gyr}}{\tau_{\text{WD}}} \right). \quad (45)$$

After obtaining T_* one can eliminate ρ in Eq. (40) by using Eqs. (42) and $\kappa = \kappa_0 \rho T^{-3.5}$, and integrate to get

$$T_* = \frac{1}{4.25} \frac{\bar{\mu}\mu_a}{k} \frac{GM_{\text{WD}}}{R_{\text{WD}}} \left(\frac{R_{\text{WD}}}{R_*} - 1 \right), \quad (46)$$

then the width of the non-degenerate WD envelope is obtained by using $R_{\text{env}} = R_{\text{WD}} - R_*$.

III. MORE DETAILS ON THE SIGNALS INDUCED BY DM IN GW DETECTORS

III.a. Signal and noise PSD for X , α and ζ combinations

Parameter	LISA	TianQin	Taiji
Arm length L (10^9 m)	2.5	0.17	3
P_{oms} (10^{-12} m)	15	1	8
P_{acc} (10^{-15} m \cdot s $^{-2}$)	3	1	3
T_{obs} (yr)	4.5	2.5	5
Frequency range (Hz)	$[10^{-4}, 1]$	$[10^{-4}, 1]$	$[10^{-4}, 1]$

Table I. The parameters of the GW detectors.

The Fourier transformation of the velocity of the satellite (21) is,

$$\frac{\tilde{\mathbf{v}}}{c}(\omega) = \frac{2\tilde{G}M}{cv_{\text{DM}}^2} \begin{bmatrix} iK_1(\omega D/v_{\text{DM}}) \\ K_0(\omega D/v_{\text{DM}}) \\ 0 \end{bmatrix}, \quad (47)$$

with $\omega = 2\pi f$. Then the Fourier transformation of Eq. (25) can be obtained,

$$\begin{aligned} \tilde{X}(\omega) = & \sqrt{\frac{2}{\pi}} \left(1 - e^{4i\omega L/c}\right) \frac{\tilde{G}M_X}{cv_{\text{DM}}^2} \sin \vartheta \times \left[K_0 \left(\frac{D\omega}{v_{\text{DM}}} \right) \sin \varphi - iK_1 \left(\frac{D\omega}{v_{\text{DM}}} \right) \cos \varphi \right] + \\ & \sqrt{\frac{8}{\pi}} \left(e^{3i\omega L/c} - e^{i\omega L/c} \right) \frac{\tilde{G}M_X}{cv_{\text{DM}}^2} \sin \vartheta \times \left[K_0 \left(\frac{D'\omega}{v_{\text{DM}}} \right) \sin \varphi - iK_1 \left(\frac{D'\omega}{v_{\text{DM}}} \right) \cos \varphi \right]. \end{aligned} \quad (48)$$

Then the signal PSD reads,

$$P(\omega) = \left\langle |\tilde{X}(\omega)|^2 \right\rangle = \frac{1}{4\pi} \int d\vartheta \sin \vartheta \int d\varphi |\tilde{X}(\omega)|^2 \quad (49)$$

$$\begin{aligned} = & \frac{32}{3\pi} \left(\frac{\tilde{G}M_X}{cv_{\text{DM}}^2} \right)^2 \sin^2(\omega L/c) \times \left\{ \left[K_0 \left(\frac{D\omega}{v_{\text{DM}}} \right) \cos(\omega L/c) - K_0 \left(\frac{D'\omega}{v_{\text{DM}}} \right) \right]^2 + \right. \\ & \left. \left[K_1 \left(\frac{D\omega}{v_{\text{DM}}} \right) \cos(\omega L/c) - K_1 \left(\frac{D'\omega}{v_{\text{DM}}} \right) \right]^2 \right\}. \end{aligned} \quad (50)$$

It can be seen that in the limit $D \ll L$, $|\mathbf{v}_2|, |\mathbf{v}_3| \ll |\mathbf{v}_1|$, and we can neglect the terms including D' in the bracket. The equation then reduces to the results given by [45].

The noise PSD for the X channel is given by expressions of the form [94]

$$S_X(f) = 16 \sin^2 \left(\frac{2\pi f L}{c} \right) \left\{ \left[3 + \cos \left(\frac{4\pi f L}{c} \right) \right] S_{\text{acc}}(f) + S_{\text{oms}}(f) \right\}, \quad (51)$$

where $S_{\text{oms}}(f)$ and $S_{\text{acc}}(f)$ denote the PSDs of the optical measurement system (OMS) and acceleration noises, respectively. The noise PSDs for LISA, TianQin, and Taiji are given by [95, 96],

$$S_{\text{oms}}(f) = \left(\frac{2\pi f P_{\text{oms}}}{c} \right)^2 \left[1 + \left(\frac{2 \times 10^{-3} \text{ Hz}}{f} \right)^4 \right] \text{Hz}^{-1} \quad (52)$$

$$S_{\text{acc}}(f) = \left(\frac{P_{\text{acc}}}{2\pi f c} \right)^2 \left[1 + \left(\frac{0.4 \times 10^{-3} \text{ Hz}}{f} \right)^2 \right] \times \left[1 + \left(\frac{f}{8 \times 10^{-3} \text{ Hz}} \right)^4 \right] \text{Hz}^{-1}, \quad (53)$$

where P_{oms} and P_{acc} are the noise amplitude parameters and their values can be found in Tab. I.

For the BBO, the noise PSDs are given by [91]

$$S_{\text{oms}}^{\text{BBO}}(f) = \frac{2.0 \times 10^{-34} \text{ m}^2}{3L^2} \text{Hz}^{-1}, \quad (54)$$

and

$$S_{\text{acc}}^{\text{BBO}}(f) = \frac{4.5 \times 10^{-34} \text{ m}^2 \cdot \text{Hz}^4}{(2\pi f)^4 (3L)^2} \text{Hz}^{-1}, \quad (55)$$

with $L = 5 \times 10^4 \text{ km}$ and $T_{\text{obs}} = 4 \text{ yr}$ for BBO.

Similar to the Michelson-like combination X, the Sagnac combination α is given by

$$\begin{aligned} \alpha(t) = & U_1(t) + V_1(t) + U_3(t - \frac{L}{c}) + V_2(t - \frac{L}{c}) + U_2(t - \frac{2L}{c}) + V_3(t - \frac{L}{c}) \\ = & -\mathbf{n}_1 \cdot \frac{\mathbf{v}(t, D) - \mathbf{v}(t - 3L/c, D)}{c} - 3\mathbf{n}_1 \cdot \frac{\mathbf{v}(t - 2L/c, D') - \mathbf{v}(t - L/c, D')}{c}, \end{aligned} \quad (56)$$

and the fully symmetric Sagnac combination ζ is

$$\begin{aligned} \zeta(t) = & U_1(t - \frac{L}{c}) + V_1(t - \frac{L}{c}) + U_2(t - \frac{L}{c}) + V_2(t - \frac{L}{c}) + U_3(t - \frac{L}{c}) + V_3(t - \frac{L}{c}) \\ = & -\mathbf{n}_1 \cdot \left[\frac{\mathbf{v}(t - L/c, D) - \mathbf{v}(t - 2L/c, D)}{c} + \frac{\mathbf{v}(t - 2L/c, D') - \mathbf{v}(t - L/c, D')}{c} \right]. \end{aligned} \quad (57)$$

After Fourier transformation, we have

$$\begin{aligned}\tilde{\alpha}(\omega) = & \sqrt{\frac{2}{\pi}} \left(1 - e^{3i\omega L/c}\right) \frac{\tilde{G}M_X}{cv_{\text{DM}}^2} \sin \vartheta \times \left[K_0 \left(\frac{D\omega}{v_{\text{DM}}} \right) \sin \varphi - iK_1 \left(\frac{D\omega}{v_{\text{DM}}} \right) \cos \varphi \right] + \\ & 3\sqrt{\frac{2}{\pi}} \left(e^{2i\omega L/c} - e^{i\omega L/c} \right) \frac{\tilde{G}M_X}{cv_{\text{DM}}^2} \sin \vartheta \times \left[K_0 \left(\frac{D'\omega}{v_{\text{DM}}} \right) \sin \varphi - iK_1 \left(\frac{D'\omega}{v_{\text{DM}}} \right) \cos \varphi \right],\end{aligned}\quad (58)$$

which leads to the PSD in the α channel,

$$\begin{aligned}P_\alpha(\omega) = \langle |\tilde{\alpha}(\omega)|^2 \rangle = & \frac{8}{3\pi} \left(\frac{\tilde{G}M_X}{cv_{\text{DM}}^2} \right)^2 \sin^2 \left(\frac{\omega L}{2c} \right) \times \left\{ \left[K_0 \left(\frac{D\omega}{v_{\text{DM}}} \right) \left(1 + 2 \cos \left(\frac{\omega L}{c} \right) \right) - 3K_0 \left(\frac{D'\omega}{v_{\text{DM}}} \right) \right]^2 + \right. \\ & \left. \left[K_1 \left(\frac{D\omega}{v_{\text{DM}}} \right) \left(1 + 2 \cos \left(\frac{\omega L}{c} \right) \right) - 3K_1 \left(\frac{D'\omega}{v_{\text{DM}}} \right) \right]^2 \right\},\end{aligned}\quad (59)$$

and

$$\begin{aligned}\tilde{\zeta}(\omega) = & \sqrt{\frac{2}{\pi}} \left(e^{i\omega L/c} - e^{2i\omega L/c} \right) \frac{\tilde{G}M_X}{cv_{\text{DM}}^2} \sin \vartheta \times \left[K_0 \left(\frac{D\omega}{v_{\text{DM}}} \right) \sin \varphi - iK_1 \left(\frac{D\omega}{v_{\text{DM}}} \right) \cos \varphi \right] + \\ & \sqrt{\frac{2}{\pi}} \left(e^{2i\omega L/c} - e^{i\omega L/c} \right) \frac{\tilde{G}M_X}{cv_{\text{DM}}^2} \sin \vartheta \times \left[K_0 \left(\frac{D'\omega}{v_{\text{DM}}} \right) \sin \varphi - iK_1 \left(\frac{D'\omega}{v_{\text{DM}}} \right) \cos \varphi \right],\end{aligned}\quad (60)$$

which leads to the PSD in the ζ channel,

$$\begin{aligned}P_\zeta(\omega) = \langle |\tilde{\zeta}(\omega)|^2 \rangle = & \frac{8}{3\pi} \left(\frac{\tilde{G}M_X}{cv_{\text{DM}}^2} \right)^2 \sin^2 \left(\frac{\omega L}{2c} \right) \times \left\{ \left[K_0 \left(\frac{D\omega}{v_{\text{DM}}} \right) - K_0 \left(\frac{D'\omega}{v_{\text{DM}}} \right) \right]^2 + \right. \\ & \left. \left[K_1 \left(\frac{D\omega}{v_{\text{DM}}} \right) - K_1 \left(\frac{D'\omega}{v_{\text{DM}}} \right) \right]^2 \right\}.\end{aligned}\quad (61)$$

The corresponding noise PSD for α and ζ channels reads,

$$S_\alpha(f) = 8 \left[2 \sin^2(\pi f L) + \sin^2(3\pi f L) \right] S_{\text{acc}}(f) + 6 S_{\text{oms}}(f), \quad (62)$$

$$S_\zeta(f) = 6 \left[4 \sin^2(\pi f L) S_{\text{acc}}(f) + S_{\text{oms}}(f) \right]. \quad (63)$$

III.b. Expected number of DM passes through the detectors for fixed SNR

In Fig. 2, we show the expected number of DM passes through the detectors $N_{\text{enc}}^{\text{GW}} = (f_X \pi D^2 \rho_{\text{DM}} v_{\text{DM}} / M_X) T_{\text{obs}}^i$ for fixed SNR=10 for LISA, Taiji, and TianQin in the X channel, with $\tilde{\alpha} = 10$. It can be seen that the expected event number is lower when the DM mass is smaller or larger. This can be understood as follows: when DM mass is smaller, the DM number density is large, and the averaged distance between DM and GW detector is small, $D \ll L$. In this case, from the Taylor expansion of Eq. (49) we get $P(\omega) \propto M_X^2 / D^2 \simeq \text{constant}$, then $N_{\text{enc}}^{\text{GW}} \propto M_X$. If the DM mass is large enough, the averaged distance satisfies $D \gg L$. After the Taylor expansion of Eq. (49) at large $D\omega/v_{\text{DM}}$, one can obtain $P(\omega) \propto \frac{M_X^2 e^{-2D\omega/v_{\text{DM}}}}{D}$ and $N_{\text{enc}}^{\text{GW}} \propto \frac{(\log M_X)^2}{M_X}$. These evaluations are both consistent with the behavior of $N_{\text{enc}}^{\text{GW}}$ in Fig. 2.

III.c. The sensitivity of GW detectors on DM in sight of astrophysical constraints for $f_X = 1$

Here we show the results where the Fermi-ball accounts for the whole DM. In this case, the DM suffers the constraints (8) from bullet cluster. The renewed constraints from WDs and NS are shown in Fig. 3. And it can be seen from Fig. 4 that the detectable range is fully excluded by the constraints from MICROSCOPE+bullet cluster. The mass limit derived from gravitational microlensing is also presented in Figs. 3 and 4. This limit relies on the fact that macroscopic DM acts as point-like lenses, as their physical size is significantly smaller than the Einstein radius [97, 98]. It is crucial to note that this constraint strictly requires $f_X = 1$. For values of $f_X \lesssim 0.01$, the limit disappears and is no longer applicable.

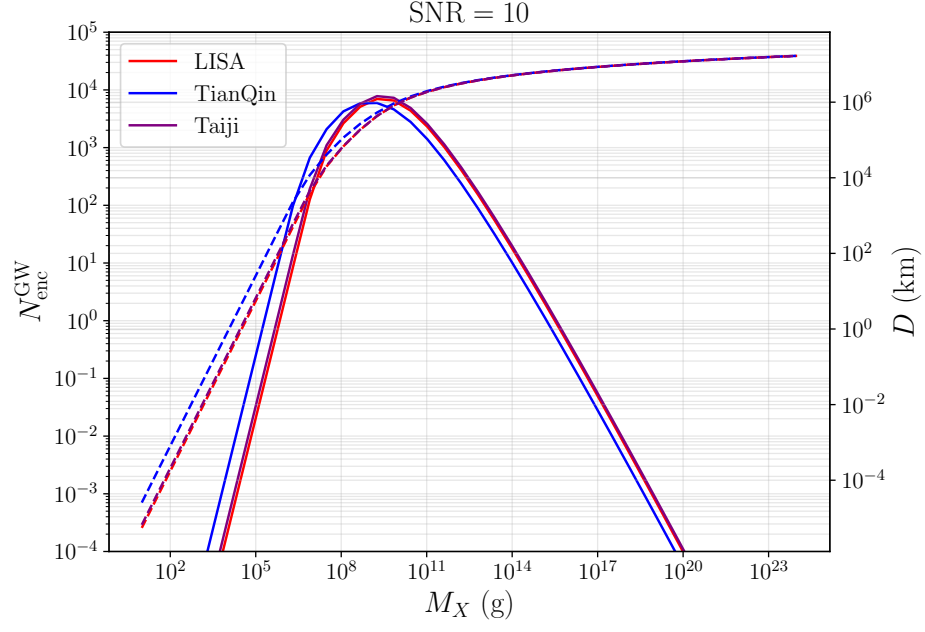


Figure 2. Expected number of DM passes through the detectors and impact factor of Fermi-ball DM as functions of DM mass in the X channel.

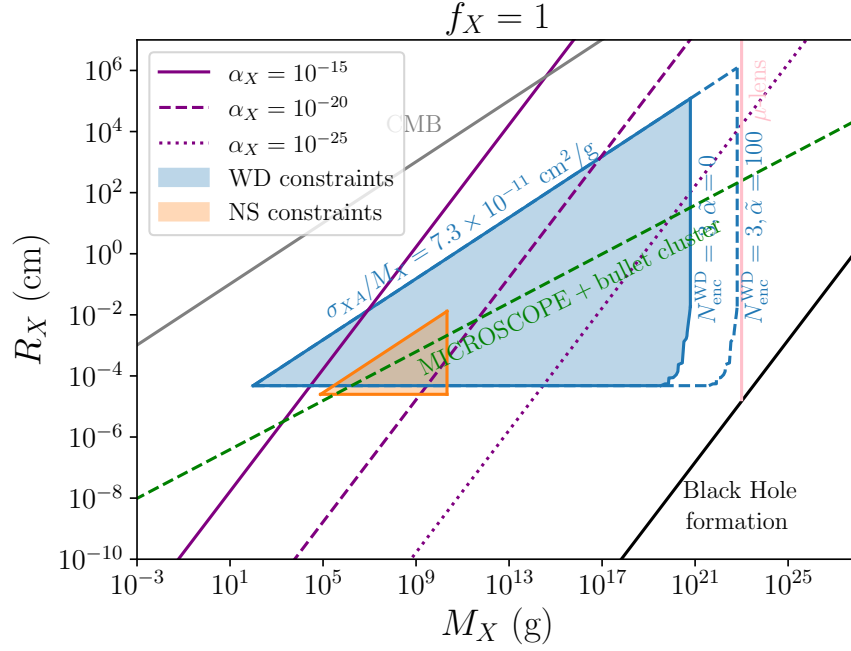


Figure 3. Constraints on Fermi-ball DM from WDs and NS. The gray line represents the CMB constraints, and the pink line denotes the constraints from microlensing.

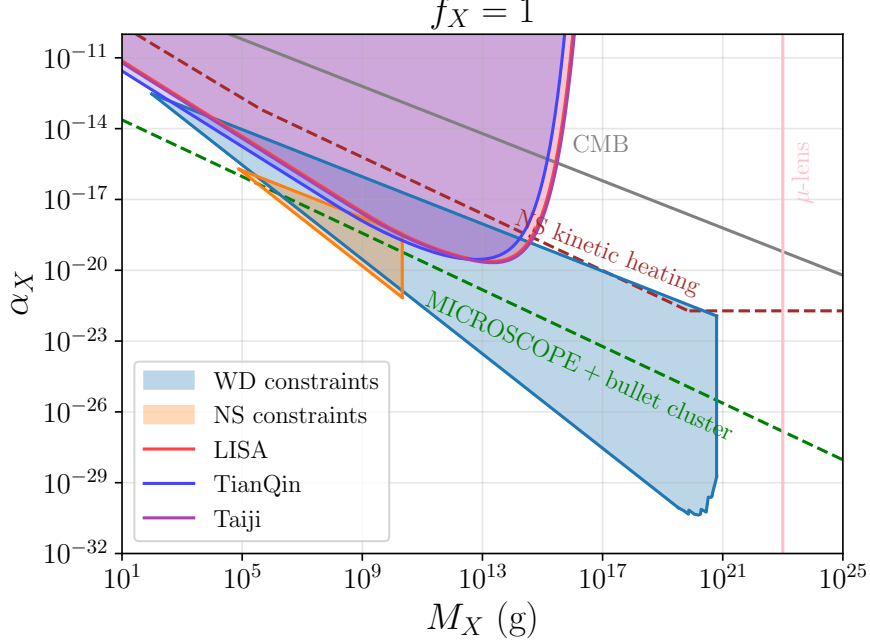


Figure 4. Sensitivity of GW detectors to Fermi-ball DM for $f_X = 1$ after taking into account the astrophysical constraints.

III.d. Full Fisher matrix analysis

The Fisher matrix approach provides a method for estimating parameter uncertainties by approximating the likelihood function as a Gaussian distribution:

$$\mathcal{L}(\theta) \propto \exp(-\theta^T \cdot \mathcal{C}^{-1} \cdot \theta / 2), \quad (64)$$

where θ is a series of model parameters.

The covariance matrix \mathcal{C} is obtained by inverting the Fisher matrix \mathcal{F} . The elements of \mathcal{F} are derived from the model of the signal $h(\theta)$, and are expressed as:

$$\mathcal{F}_{ij} = \sum_{k=X,\alpha,\zeta} \langle \partial_{\theta_i} h^k | \partial_{\theta_j} h^k \rangle. \quad (65)$$

In this work, we simply set the signal h to be $\sqrt{P(f)}$. The inner product is defined as follows:

$$\langle a | b \rangle = 4 \int_0^\infty df \frac{\Re(a(f)b^*(f))}{S_n(f)} \quad (66)$$

with $S_n(f)$ being the instrument noise PSD. The numerical challenge is connected to the inversion of the Fisher matrix. This issue comes from the large range of numerical values, e.g., large values of DM mass and small values of α_X . So we choose the parameter set to be $\{\log_{10}(M_X/g), \log_{10} \alpha_X, \log_{10}(D/\text{km}), v_{\text{DM}}(\text{km/s})\}$.

Fig. 5 and Fig. 6 present the projected 68% and 95% confidence level (CL) contours for a DM signal for TianQin and LISA+Taiji, respectively. The analysis assumes a fiducial parameter set of $\{\log_{10}(M_X/g) = 8, \log_{10} \alpha_X = -13.5, \log_{10}(D/\text{km}) = 1, v_{\text{DM}}(\text{km/s}) = 220\}$. In this visualization, the diagonal panels display the one-dimensional marginalized posterior distributions, while the off-diagonal panels reveal the two-dimensional covariance ellipses. The numerical values above each column indicate the inferred means and 1σ uncertainties derived from the Fisher matrix analysis.

The results demonstrate that TianQin can constrain the signal parameters with remarkable precision. Specifically, the DM mass M_X is determined with a relative error of approximately 44% (at 68% CL). This tight constraint is

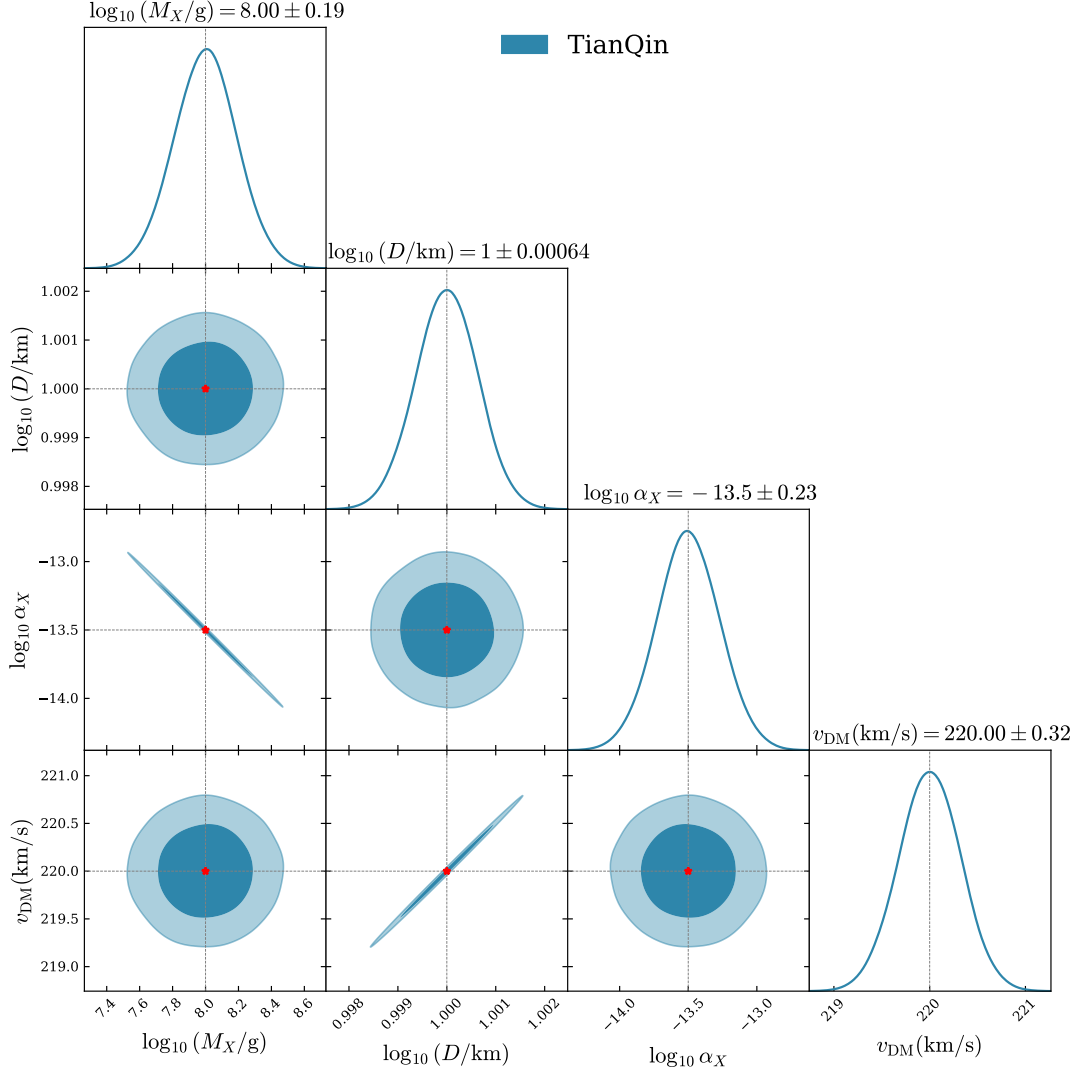


Figure 5. Triangle plot of the Fisher analysis for a signal at TianQin induced by Fermi-ball DM.

anticipated, given the high sensitivity of the GW signal phase to the underlying DM mass. The distance parameter D/km is constrained with a relative precision of $\sim 0.15\%$. Similarly, the dark matter velocity v_{DM} is determined with a relative error of $\sim 0.15\%$. This sub-percent precision indicates that TianQin is highly sensitive to the spectral features governed by the velocity and the distance. In contrast, the coupling strength α_X exhibits a larger uncertainty. The comparatively looser constraint on $\log_{10}\alpha_X$ —despite the high precision on $\log_{10}M_X$ —suggests that the intrinsic coupling strength suffers from partial degeneracies with the dark matter mass. A notable correlation is observed between the coupling strength $\log_{10}\alpha_X$ and the DM mass $\log_{10}M_X$, as evidenced by the upward-left tilt (negative correlation) of the corresponding contour. Consequently, a source placed at a larger DM mass $\log_{10}M_X$ can produce the same observed signal strength if it possesses a lower $\log_{10}\alpha_X$. We also observe the degeneracy between the velocity v_{DM} and the distance $\log_{10}(D/\text{km})$, as evidenced by the elongated contours in the corresponding subplot (upward-right).

We further explore the parameter reconstruction capabilities of LISA (blue contours) and Taiji (red contours) in Fig. 6. We have separated these results from TianQin due to the distinct PSDs. Overall, the comparative results for both detectors exhibit similar qualitative behaviors, although the resulting uncertainties are generally larger than those obtained for TianQin. LISA exhibits visibly tighter confidence regions across the entire parameter space relative to Taiji. This difference is likely due to the specific signal falling closer to the optimal sensitivity band of LISA. The strong degeneracy between the coupling strength $\log_{10}\alpha_X$ and the distance $\log_{10}(D/\text{km})$ persists in both cases. Other parameter pairs also display distinct elliptical shapes, indicating their correlations.

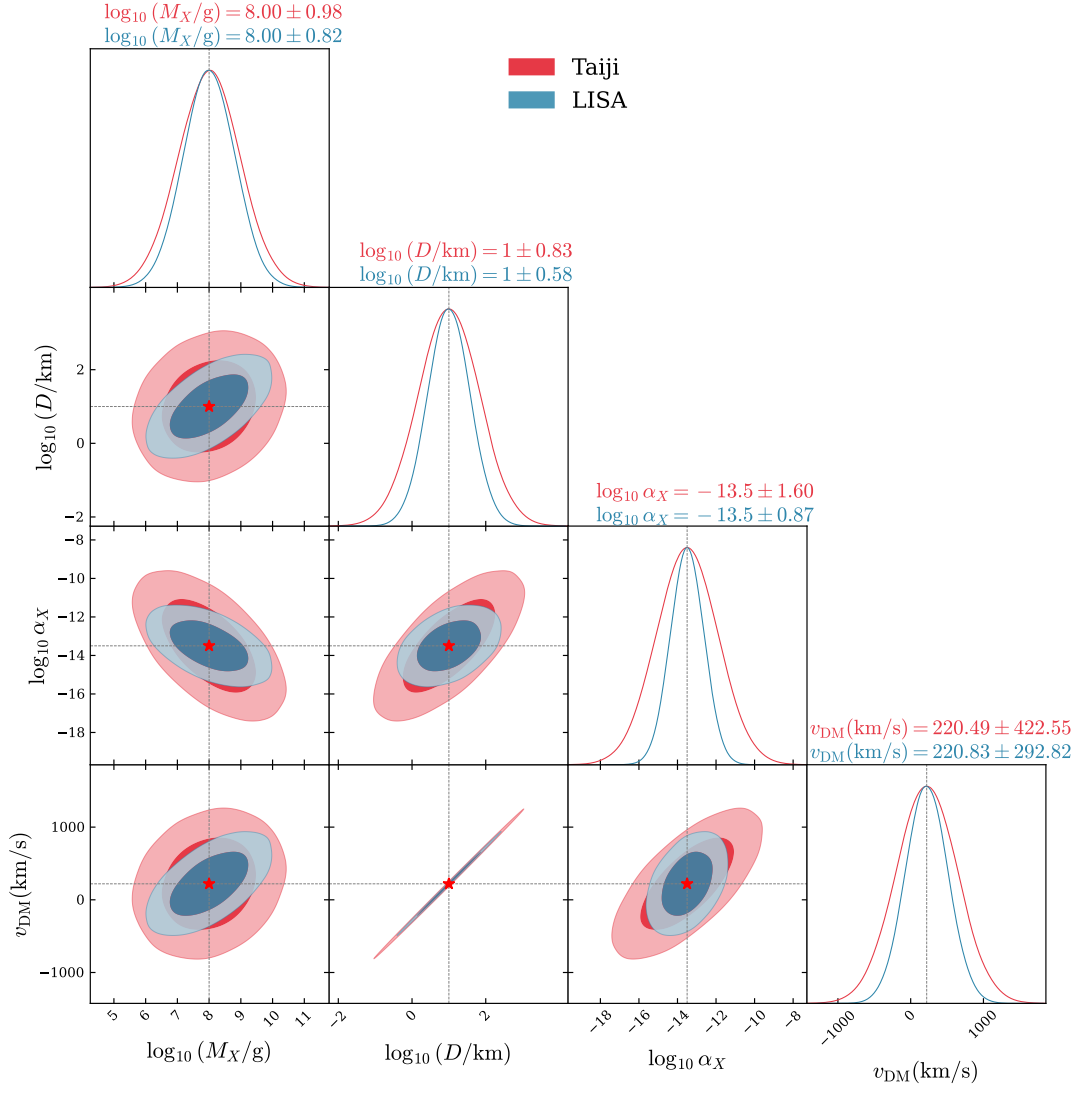


Figure 6. Triangle plot of the Fisher analysis for a signal at LISA and Taiji induced by Fermi-ball DM.